NATIONAL ENERGY TECHNOLOGY LABORATORY

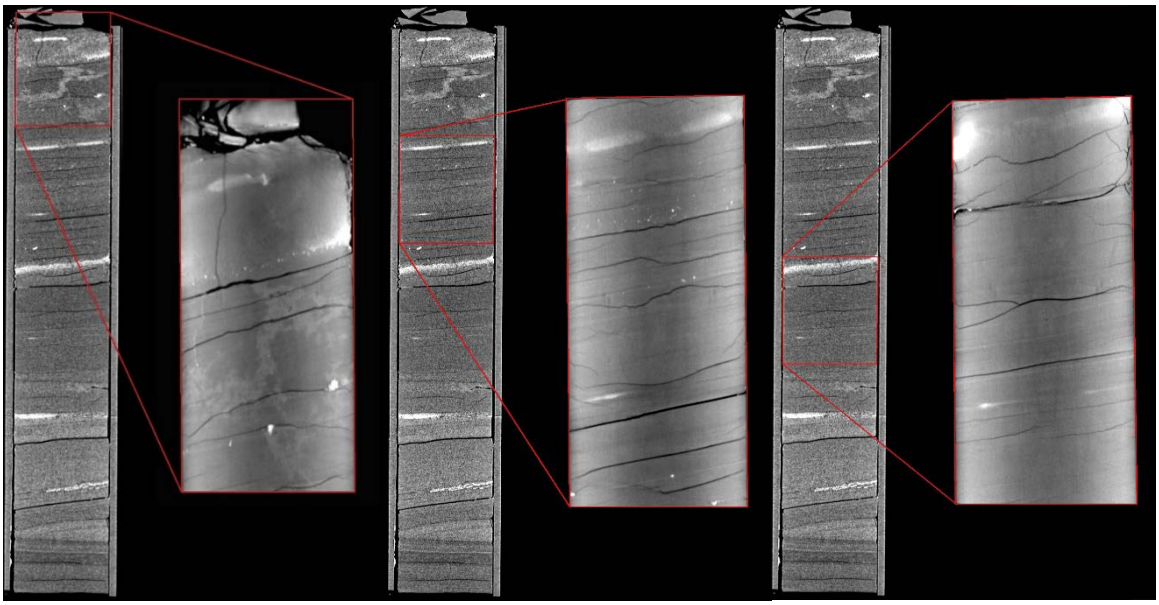

Computed Tomography Scanning and Geophysical Measurements of Core from the Marcellus Shale Energy and Environment Laboratory

21 December 2018

U.S. DEPARTMENT OF ENERGY | NATIONAL ENERGY TECHNOLOGY LABORATORY

Office of Fossil Energy

NETL-TRS-22-2018

Disclaimer

Cover Illustration: Reconstructed images from NETL's medical computed tomography (CT) scanner of core within 4-in. diameter core barrels from Marcellus Shale Energy and Environment Laboratory (MSEEL), obtained from a depth of 7,553 to 7,555 ft. Red boxes represent reconstructed images from NETL's industrial CT scanner of core within 4-in. diameter core barrels from MSEEL, obtained from 7,553 to 7,554.6 ft.

Suggested Citation: Paronish, T.; Mackey, P.; Crandall, D.; Moore, J.; Brown, S.; Carr, T.; Martin, K. *Computed Tomography Scanning and Geophysical Measurements of Core from the Marcellus Shale Energy and Environment Laboratory*; NETL-TRS-22-2018; NETL Technical Report Series; U.S. Department of Energy, National Energy Technology Laboratory: Morgantown, WV, 2018; p 56. DOI: 10.18141/1488537.

An electronic version of this report can be found at:

https://netl.doe.gov/research/on-site-research/publications/featured-technical-reports

https://edx.netl.doe.gov/ucr

The data in this report can be accessed from NETL's Energy Data eXchange (EDX) online system (https://edx.netl.doe.gov) using the following link: https://edx.netl.doe.gov/dataset/MIP3H-Scans

Computed Tomography Scanning and Geophysical Measurements of Core from the Marcellus Shale Energy and Environment Laboratory

Thomas Paronish[1,2], Paige Mackey[1,2], Dustin Crandall[1], Johnathan Moore[1,3], Sarah Brown[1,3], Tim Carr[4], Keithan Martin[4]

[1]U.S. Department of Energy, National Energy Technology Laboratory, 3610 Collins Ferry Road, Morgantown, WV 26507

[2]U.S. Department of Energy, National Energy Technology Laboratory, ORISE, 3610 Collins Ferry Road, Morgantown, WV 26507

[3]U.S. Department of Energy, National Energy Technology Laboratory, AECOM, 3610 Collins Ferry Road, Morgantown, WV 26507

[4]West Virginia University, Department of Geology and Geography, 98 Beechurst Avenue, Morgantown, WV 26506

NETL-TRS-22-2018

21 December 2018

NETL Contacts:

Dustin Crandall, Principal Investigator

Alexandra Hakala, Technical Portfolio Lead

Bryan Morreale, Executive Director, Research & Innovation Center

This page intentionally left blank

Table of Contents

List of Figures

List of Figures (cont.)

List of Figures (cont.)

List of Tables

Acronyms, Abbreviations, and Symbols

Term	Description
2D	Two -dimensional
3D	Three-dimensional
API	American Petroleum Institute
BBL	Billion barrels
CT	Computed tomography
DOE	U.S. Department of Energy
EDX	NETL's Energy Data eXchange
IGSN	International Geo Sample Number
MSCL	Multi-Sensor Core Logger
MSEEL	Marcellus Shale Energy and Environment Laboratory
NETL	National Energy Technology Laboratory
NNE	Northeast Natural Energy
SESAR	System for Earth Science Sample Registration
Tcf	Trillion cubic feet
TOC	Total organic carbon
XRF	X-ray fluorescence

Acknowledgments

This work was completed at the National Energy Technology Laboratory (NETL) with support from U.S. Department of Energy's (DOE) Office of Fossil Energy Oil & Gas Program. The authors wish to acknowledge Bryan Morreale and Alexandra Hakala (NETL Research & Innovation Center), Jared Ciferno, (NETL Technology Development and Integration Center), and Elena Melchert (DOE Office of Fossil Energy) for programmatic guidance, direction, and support.

The authors would like to thank Bryan Tennant, Karl Jarvis, and Roger Lapeer for making the CT scanner lab functional. Thank you to Robert Vagnetti (Program Manager at NETL) for ensuring this research could be performed. Thank you to Dustin McIntyre and Mark McKoy for laboratory support. This research was supported in part by appointments from the NETL Research Participation Program, sponsored by the U.S. DOE, and administered by the Oak Ridge Institute for Science and Education.

ABSTRACT

The computed tomography (CT) facilities and the Multi-Sensor Core Logger (MSCL) at the National Energy Technology Laboratory (NETL) in Morgantown, West Virginia were used to characterize middle Devonian black shale from the Marcellus Shale Energy and Environmental Laboratory (MSEEL) site in northeastern West Virginia. The samples are representative of the Middle Devonian Marcellus Formation, a clay-rich black shale in the Appalachian Basin. The MSEEL site is a unique field study area for new techniques supporting natural gas production and a high level of monitoring of environmental impacts. The primary impetus of this work is a collaboration between NETL, West Virginia University, Northeast Natural Energy (NNE), and Ohio State University to characterize core from multiple wells to better understand the structure and variation of the Marcellus Shale formations. This report, and the associated scans, provide detailed datasets not typically available from unconventional shales for analysis. The resultant datasets are presented as part of this report and can be accessed from NETL's Energy Data eXchange (EDX) online system (https://edx.netl.doe.gov) using the following link: https://edx.netl.doe.gov/dataset/MIP3H-Scans.

All equipment and techniques used were non-destructive, enabling future examinations to be performed on these cores. None of the equipment used was suitable for direct visualization of the shale pore space, although fractures and discontinuities were detectable with the methods tested. High resolution CT imagery with the NETL industrial CT scanner was a powerful and insightful way to examine the details of fractures, discontinuities, minerals, and large crystals within the shale, but was time consuming both in collection and analysis. As such, only a small percentage of the core was scanned at high resolution. Low resolution CT imagery with the NETL medical CT scanner was performed on the entire core. Qualitative analysis of the medical CT images, coupled with the measurements from the X-ray fluorescence (XRF), P-wave, and magnetic susceptibility of the MSCL were useful in identifying zones of interest for more detailed analysis and locating fractured zones. The ability to quickly identify key areas for more detailed study with higher resolution will save time and resources in future studies. The combination of all methods used provides a multi-scale analysis of the core; the resulting description of the core is relevant for many subsurface energy related examinations of core that have traditionally been performed at NETL.

1. INTRODUCTION

The Middle Devonian Marcellus Formation, with the development of hydraulic fracturing and horizontal drilling, has become one of the most prolific shale plays in the world. The Marcellus play has a lateral extent of 21,266 mi^2 (55,078.7 km^2) in the Appalachian basin and has an estimated technically recoverable resource of 309.0 trillion cubic feet (Tcf) of natural gas with an additional 14.0 billion barrels (BBL) of natural gas liquids (EIA, 2018). Given the potential of the Marcellus Shale as a long-term major producer of gas and gas liquids, it is important to better understand and utilize best practices to identify and produce the resource economically and to do so in an environmentally responsible manner. Under these principles, the Marcellus Shale Energy and Environmental Laboratory (MSEEL) project was founded to pursue a better understanding of the Marcellus Shale by utilizing new technologies to optimize production and reduce the environmental impact. The MSEEL project is a joint venture between the U.S. Department of Energy's (DOE) National Energy Technology Laboratory (NETL), West Virginia University, Northeast Natural Energy, and Ohio State University.

1.1 SITE OVERVIEW

The MSEEL project is located in the Morgantown Industrial Park, Monongalia County, West Virginia. The project site originally included two lateral Marcellus wells drilled in the summer of 2011: the MIP-4H pilot and lateral well (API 47-061-01622) and the MIP-6H lateral well (API 47-061-01624). Through the MSEEL project three additional wells targeting the Marcellus Shale were drilled in the fall of 2015: the MIP-SW pilot (API 47-061-01705); MIP-5H lateral (API 47-061-01699); and MIP-3H pilot and lateral (API 47-061-01707) which is the focus for this report. Figure 1 displays the site layout and location in the Appalachian basin.

The MIP-3H well (API 47-061-01707) geographic coordinates are: latitude 39.602203 N, longitude -79.976624 W (Figure 1). The Marcellus Shale is approximately 100 ft (30.5 m) thick and occurs at a measured depth of approximately 7,447 ft (2,269.85 m). Approximately 112 ft of core was recovered from the MIP-3H well at a depth from 7,445 ft to 7,557 ft (2,269.2 to 2,303.4 m); this encompasses strata from the upper Onondaga to the lower portion of the Mahantango. The core was slabbed into 1/3 and 2/3 sections. The 1/3 section was preserved for archival purposes and non-destructive testing; the 2/3 section was intended to be utilized for destructive experiments. This core along with additional sidewall core samples from MIP-SW (API 47-061-01705) are described in this report.

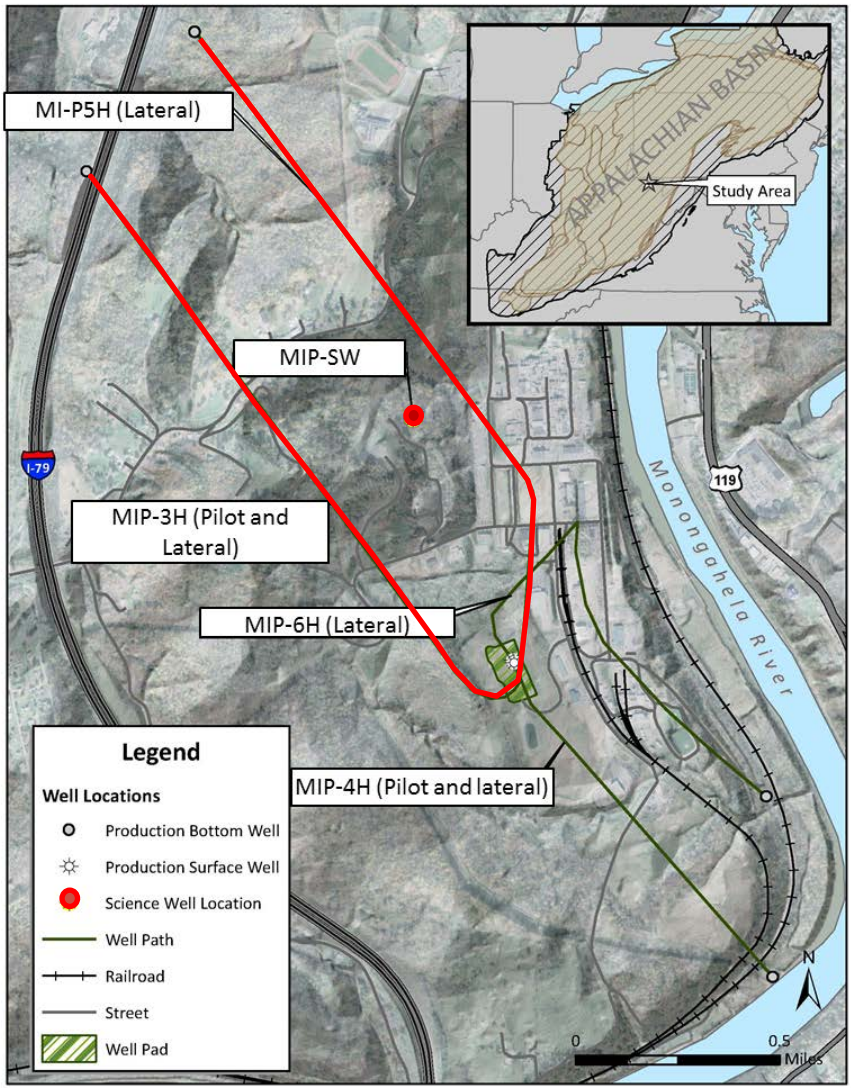

Figure 1: Morgantown Industrial Park Pad layout. Green indicates wells drilled in the summer of 2011. Red outline area indicates wells associated with the MSEEL project (MSEEL.org).

1.2 GEOLOGICAL BACKGROUND

1.2.1 Basin History

During the Middle Devonian, the Acadian orogeny accommodated oblique collision between the Avalonian terrain and the Laurentian terrain (Ettensohn, 1985). This oblique collision provided closure of the basin to the south and east by the Acadian Mountains and to the west and north by the Cincinnati Arch fore-bulge (Williams and Hatcher, 1982; Ettensohn, 1985; Brett and Baird, 1996). This enclosure and the ongoing collision ended shallow shelf carbonate deposition and allowed for accommodation of the organic-rich shale units of the Catskill delta (Lash and Engelder, 2011).

The mode and direction of sedimentation was influenced by the paleogeographic location and paleoclimate. At this time, the Appalachian basin was located east-west at approximately 30-35° S of the Devonian equator (Witzke and Heckel, 1988). This paleogeography placed the basin in a subtropical zone between subtropical trade winds and its close proximity to the horse latitudes resulting in seasonal variation between dry conditions and stormy conditions (Figure 2).

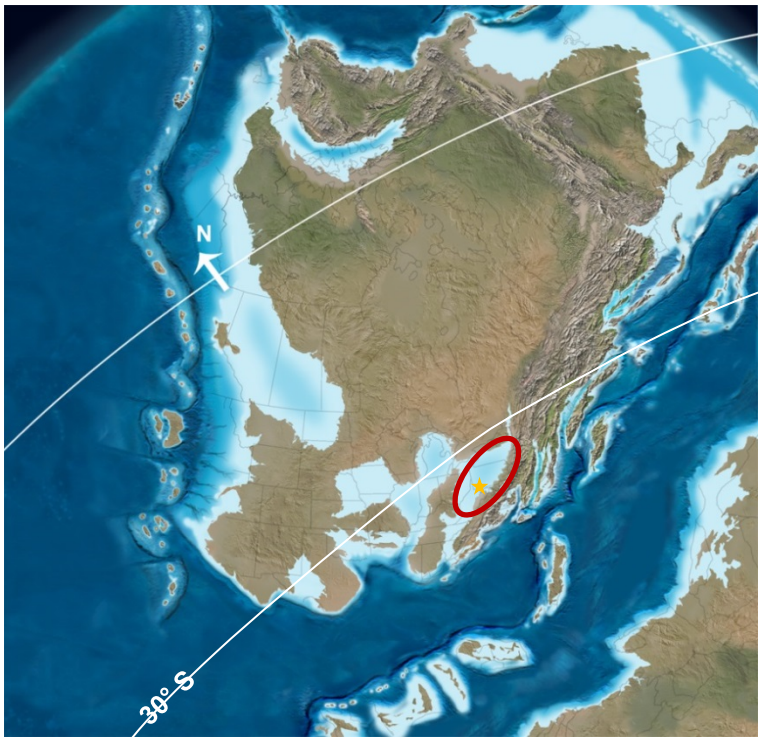

Figure 2: Middle Devonian paleogeography, red circle indicates the position of the Appalachian basin with the Arcadian mountains to the south and the Cincinnati arch to the north, The yellow star indicates our study location, and the white lines indicate the approximate orientation of the paleo-equator and 30° S latitude according to Witzke and Heckel (1988) (modified from Blakey, 2010).

1.2.2 Sedimentation and Stratigraphy

The MSEEL project's focus is on the Marcellus Formation. The Marcellus Formation is a Middle Devonian (Eifelian to Givetian) mudstone at the base of the Hamilton Group. The Marcellus Formation is underlain by the crystalline limestone Onondaga Formation and overlain by the clay-rich dark grey shale of the Mahantango Formation.

The Marcellus Formation in the study area is expected to be found at a depth of approximately 7,400 ft (2,255.52 m) and to be approximately 100 ft (30.5 m) thick (Figure 3) (Boyce and Carr, 2009). The study area sits in the middle of the "high gas" fairway (Figure 4), which was determined to be where the thickness of Marcellus Shale is greater than 230 API (American Petroleum Institute units). This cutoff is established through the linear relationship between gamma-ray and total organic carbon (TOC), as seen in Figure 4.

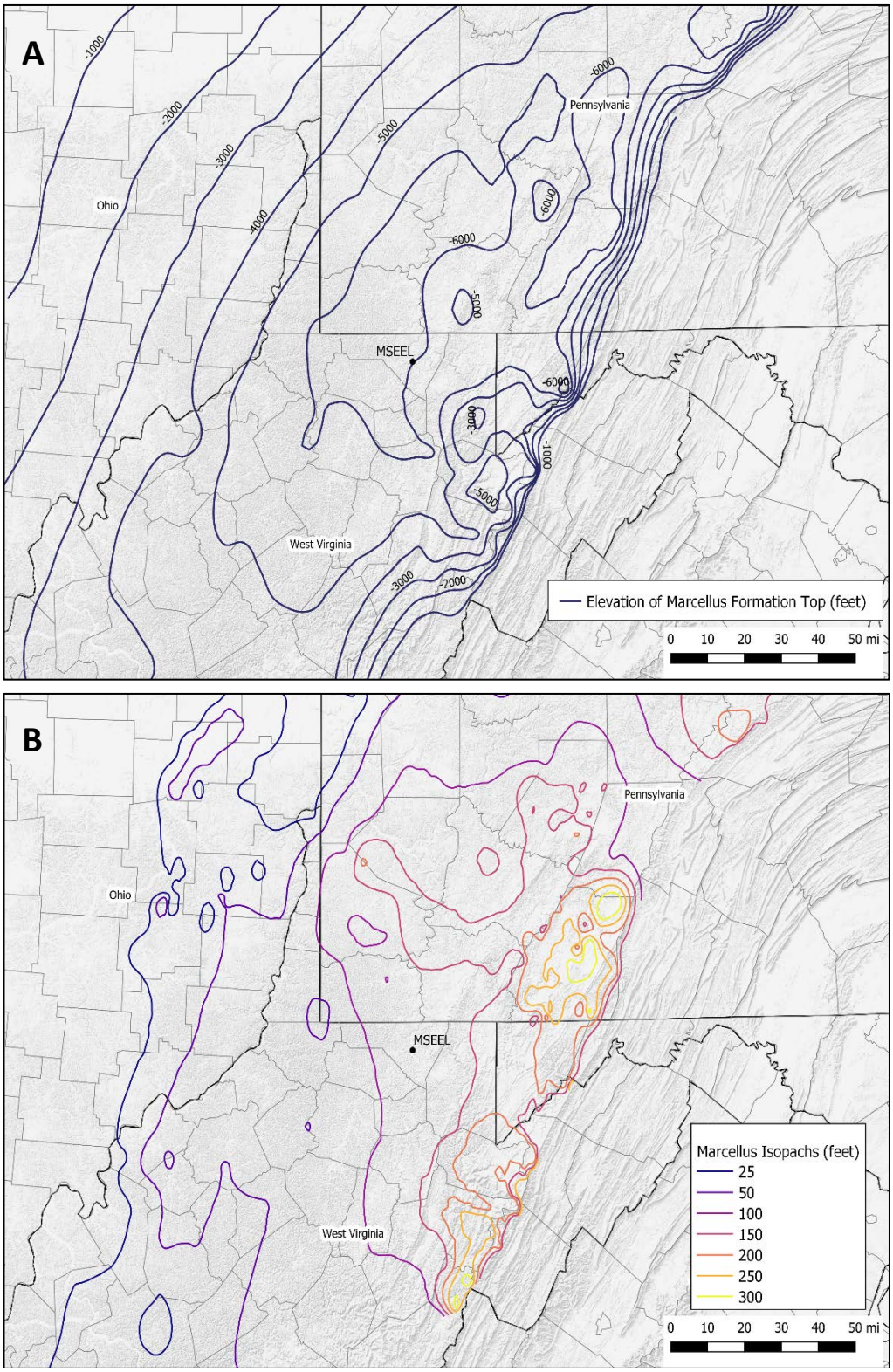

Figure 3: (A) Structure map for the top of the Marcellus Formation, the black dot denotes the study area and sits 6,000 ft below mean sea level; (B) Marcellus isopach map, the black dot denotes the study area. Generally, the Marcellus Formation decreases in thickness from about 300 ft in the east to about 25 ft in the west.

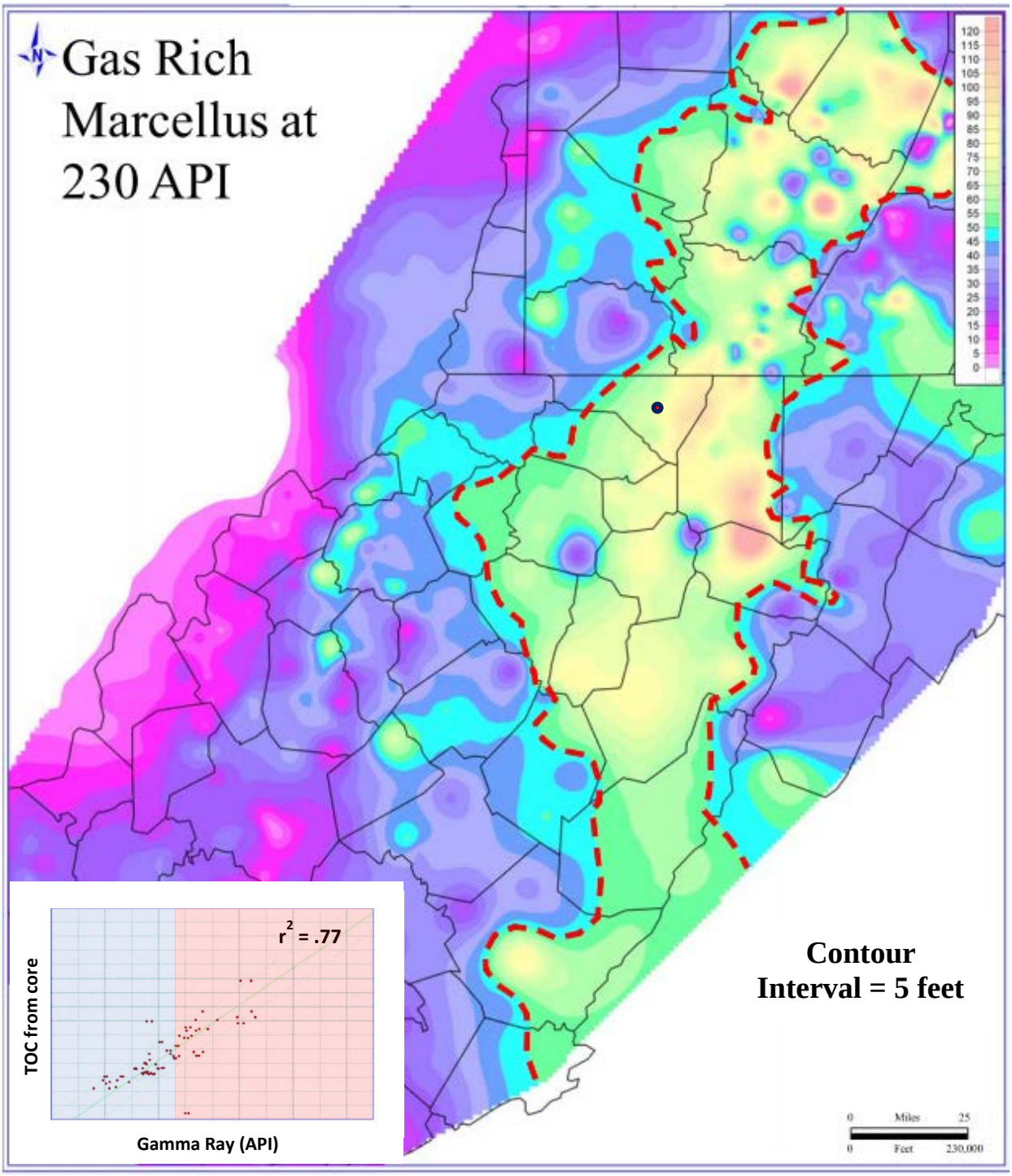

Figure 4: Gas-rich Marcellus map; net thickness of Marcellus Shale with greater than 230 API gamma ray units. The red dashed line denotes the gas rich Marcellus fairway running approximately north to south. The cross-plot shows TOC from core vs. gamma-ray, blue shading indicates the interval of low gamma-ray (< 230 API) and red shading indicates high gamma-ray values (≥ 230 API). Modified from Boyce and Carr (2009).

2. CORE DESCRIPTION

The methods established for fine-grained sedimentary rocks by Lazar et al. (2015) were used to describe the MIP-3H core. The core was described in two passes, the first focused on determining “texture” and “composition”. Texture being the amount of silt-sized quartz grains present and is defined as coarse, medium, or fine silt-sized grains. Composition of the mudstone is defined by the amount of quartz, carbonate, and clay present and is categorized as siliceous, calcareous, and argillaceous, respectively. The second determination focused on sedimentary and structural features present in the core. These features include the identification of fracture type and intensity, nodules, concretions, bedding, other fabric, fossils, and bioturbation (Lazar et al., 2015). The second pass was aided by the medical CT scans to identify fracture structures and morphology in a three-dimensional (3D) prospective.

These cores were entered in the System for Earth Science Sample Registration (SESAR), a registry that catalogs and preserves sample data and allows access for industry, academic institutions, researchers, and the public to view this data online (IEDA, 2018). Each core box is assigned an International Geo Sample Number (IGSN) which allows unique identification and referencing. These listings for the MIP-3H well and sidewall cores are shown in Table 1.

The rock is made of medium grey to dark-grey, argillaceous shale, that transitions into dark-grey to black, siliceous, organic-rich shale, becoming calcareous and fossil-rich at the base of the cored interval. Calcite concretions are present intermittently throughout the well with an increase in frequency from 7,529.45 to 7,531.2 ft (2,294.98 to 2,295.5 m). Pyrite nodules are present throughout the well, with a slight increase in the degree of pyritization with increasing depth. Bioturbation and fracture zones are found in the cored interval as well. Figure 5 shows a detailed description of the cored interval.

Table 1: SESAR IGSN Sample Names

Field Name	IGSN	Link
MSEEL MIP 3H C1 B1	IENTL0102	https://app.geosamples.org/sample/igsn/IENTL0102
MSEEL MIP 3H C1 B2	IENTL0103	https://app.geosamples.org/sample/igsn/IENTL0103
MSEEL MIP 3H C1 B3	IENTL0104	https://app.geosamples.org/sample/igsn/IENTL0104
MSEEL MIP 3H C1 B4	IENTL0105	https://app.geosamples.org/sample/igsn/IENTL0105
MSEEL MIP 3H C1 B5	IENTL0106	https://app.geosamples.org/sample/igsn/IENTL0106
MSEEL MIP 3H C1 B6	IENTL0107	https://app.geosamples.org/sample/igsn/IENTL0107
MSEEL MIP 3H C1 B7	IENTL0108	https://app.geosamples.org/sample/igsn/IENTL0108
MSEEL MIP 3H C1 B8	IENTL0109	https://app.geosamples.org/sample/igsn/IENTL0109
MSEEL MIP 3H C1 B9	IENTL010A	https://app.geosamples.org/sample/igsn/IENTL010A
MSEEL MIP 3H C1 B10	IENTL010B	https://app.geosamples.org/sample/igsn/IENTL010B
MSEEL MIP 3H C1 B11	IENTL010C	https://app.geosamples.org/sample/igsn/IENTL010C
MSEEL MIP 3H C1 B12	IENTL010D	https://app.geosamples.org/sample/igsn/IENTL010D
MSEEL MIP 3H C1 B13	IENTL010E	https://app.geosamples.org/sample/igsn/IENTL010E
MSEEL MIP 3H C1 B14	IENTL010F	https://app.geosamples.org/sample/igsn/IENTL010F
MSEEL MIP 3H C1 B15	IENTL010G	https://app.geosamples.org/sample/igsn/IENTL010G
MSEEL MIP 3H C1 B16	IENTL010H	https://app.geosamples.org/sample/igsn/IENTL010H
MSEEL MIP 3H C1 B17	IENTL010I	https://app.geosamples.org/sample/igsn/IENTL010I
MSEEL MIP 3H C1 B18	IENTL010J	https://app.geosamples.org/sample/igsn/IENTL010J
MSEEL MIP 3H C1 B19	IENTL010K	https://app.geosamples.org/sample/igsn/IENTL010K
MSEEL MIP 3H C1 B20	IENTL010L	https://app.geosamples.org/sample/igsn/IENTL010L
MSEEL MIP 3H C1 B21	IENTL010M	https://app.geosamples.org/sample/igsn/IENTL010M
MSEEL MIP 3H C1 B22	IENTL010N	https://app.geosamples.org/sample/igsn/IENTL010N
MSEEL MIP 3H C1 B23	IENTL010O	https://app.geosamples.org/sample/igsn/IENTL010O
MSEEL MIP 3H C1 B24	IENTL010P	https://app.geosamples.org/sample/igsn/IENTL010P
MSEEL MIP 3H C1 B25	IENTL010Q	https://app.geosamples.org/sample/igsn/IENTL010Q
MSEEL MIP 3H C1 B26	IENTL010R	https://app.geosamples.org/sample/igsn/IENTL010R
MSEEL MIP 3H C1 B27	IENTL010S	https://app.geosamples.org/sample/igsn/IENTL010S
MSEEL MIP 3H C1 B28	IENTL010T	https://app.geosamples.org/sample/igsn/IENTL010T
MSEEL MIP 3H C1 B29	IENTL010U	https://app.geosamples.org/sample/igsn/IENTL010U
MSEEL MIP 3H C1 B30	IENTL010V	https://app.geosamples.org/sample/igsn/IENTL010V
MSEEL MIP 3H C1 B31	IENTL010W	https://app.geosamples.org/sample/igsn/IENTL010W
MSEEL MIP 3H C1 B32	IENTL010X	https://app.geosamples.org/sample/igsn/IENTL010X
MSEEL MIP 3H C1 B33	IENTL010Y	https://app.geosamples.org/sample/igsn/IENTL010Y
MSEEL MIP 3H C1 B34	IENTL010Z	https://app.geosamples.org/sample/igsn/IENTL010Z
MSEEL MIP 3H C1 B35	IENTL0110	https://app.geosamples.org/sample/igsn/IENTL0110
MSEEL MIP 3H C1 B36	IENTL0111	https://app.geosamples.org/sample/igsn/IENTL0111
MSEEL MIP 3H C1 B37	IENTL0112	https://app.geosamples.org/sample/igsn/IENTL0112
MSEEL MIP 3H C1 B38	IENTL0113	https://app.geosamples.org/sample/igsn/IENTL0113
MSEEL MIP 3H C1 B39	IENTL0114	https://app.geosamples.org/sample/igsn/IENTL0114
MSEEL MIP 3H C1 B40	IENTL0115	https://app.geosamples.org/sample/igsn/IENTL0115
MSEEL MIP 3H C1 B41	IENTL0116	https://app.geosamples.org/sample/igsn/IENTL0116
MSEEL 1/3rd MIP 3H C1 B 1	IENTL0117	https://app.geosamples.org/sample/igsn/IENTL0117
MSEEL 1/3rd MIP 3H C1 B 2	IENTL0118	https://app.geosamples.org/sample/igsn/IENTL0118
MSEEL 1/3rd MIP 3H C1 B 3	IENTL0119	https://app.geosamples.org/sample/igsn/IENTL0119
MSEEL 1/3rd MIP 3H C1 B 4	IENTL011A	https://app.geosamples.org/sample/igsn/IENTL011A
MSEEL 1/3rd MIP 3H C1 B 5	IENTL011B	https://app.geosamples.org/sample/igsn/IENTL011B

Table 1: SESAR IGSN Sample Names (cont.)

Field Name	IGSN	Link
MSEEL 1/3rd MIP 3H C1 B 6	IENTL011C	https://app.geosamples.org/sample/igsn/IENTL011C
MSEEL 1/3rd MIP 3H C1 B 7	IENTL011D	https://app.geosamples.org/sample/igsn/IENTL011D
MSEEL 1/3rd MIP 3H C1 B 8	IENTL011E	https://app.geosamples.org/sample/igsn/IENTL011E
MSEEL 1/3rd MIP 3H C1 B 9	IENTL011F	https://app.geosamples.org/sample/igsn/IENTL011F
MSEEL 1/3rd MIP 3H C1 B 10	IENTL011G	https://app.geosamples.org/sample/igsn/IENTL011G
MSEEL 1/3rd MIP 3H C1 B 11	IENTL011H	https://app.geosamples.org/sample/igsn/IENTL011H
MSEEL 1/3rd MIP 3H C1 B 12	IENTL011I	https://app.geosamples.org/sample/igsn/IENTL011I
MSEEL sidewall Run #1, MIP-SW	IENTL0120	https://app.geosamples.org/sample/igsn/IENTL0120
MSEEL sidewall Run #2, MIP-SW	IENTL0121	https://app.geosamples.org/sample/igsn/IENTL0121
MSEEL sidewall Run #3, MIP-SW	IENTL0122	https://app.geosamples.org/sample/igsn/IENTL0122
MSEEL sidewall Run #4, MIP-SW	IENTL0123	https://app.geosamples.org/sample/igsn/IENTL0123

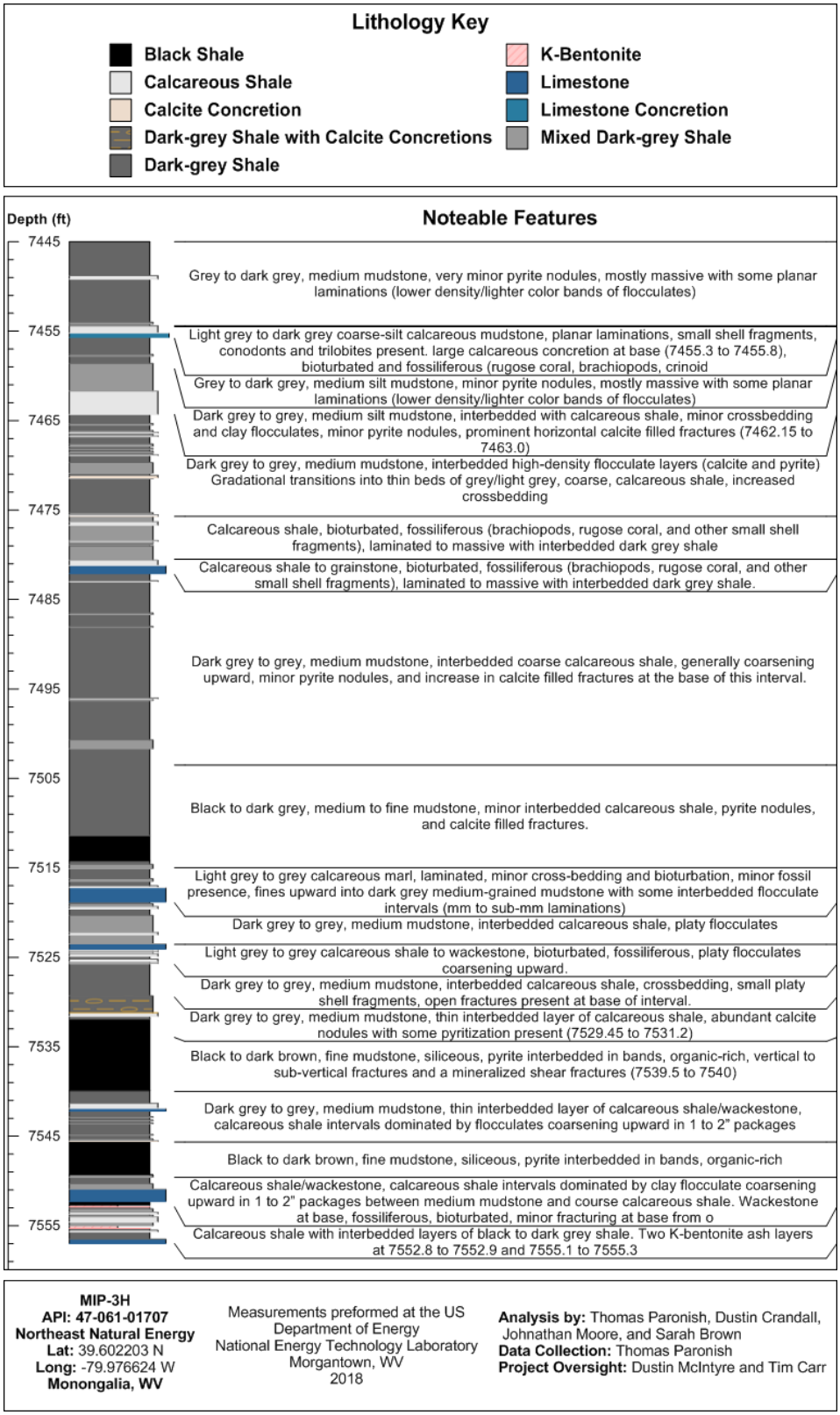

Figure 5: Detailed core description for MIP-3H from 7,445 to 7,557 ft.

2.1 CORE PHOTOGRAPHS

Photographs of the 1/3 slabbed core are shown in Figures 6 through 17.

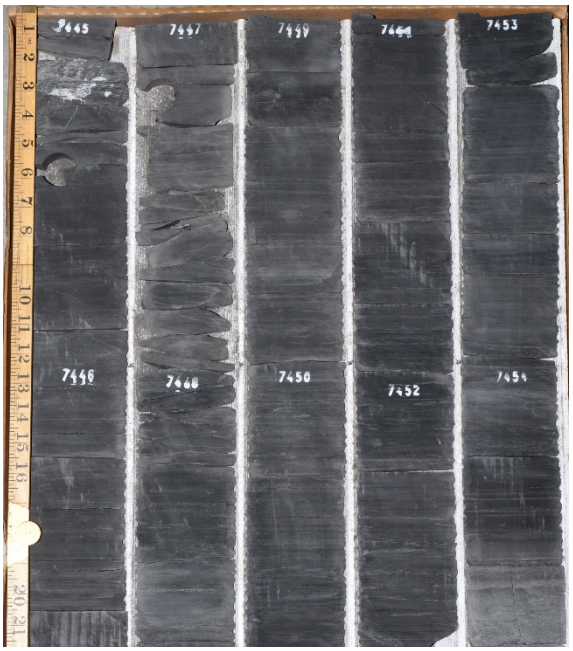

Figure 6: MIP-3H core photographs, from 7,445 to 7,455 ft.

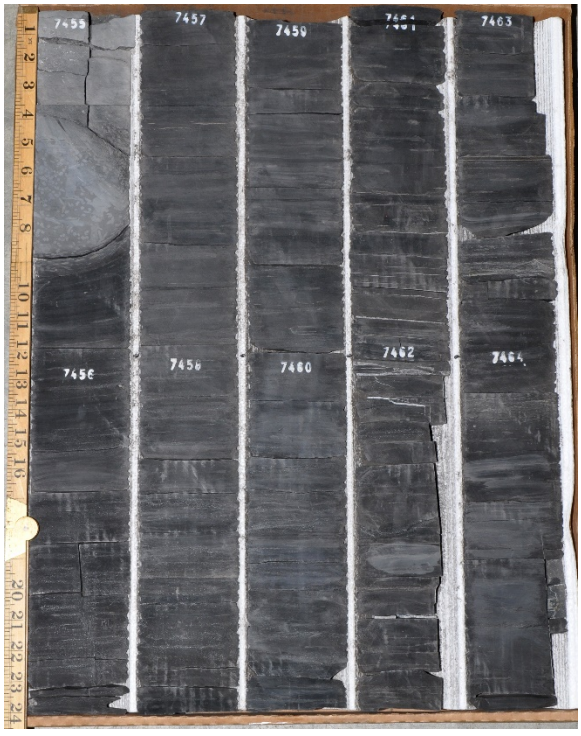

Figure 7: MIP-3H core photographs, from 7,455 to 7,465 ft.

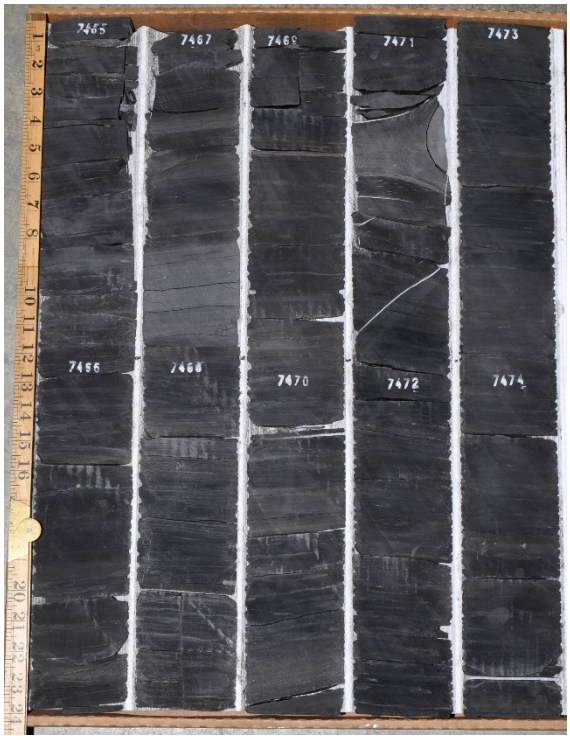

Figure 8: MIP-3H core photographs, from 7,465 to 7,475 ft.

Figure 9: MIP-3H core photographs, from 7,475 to 7,485 ft.

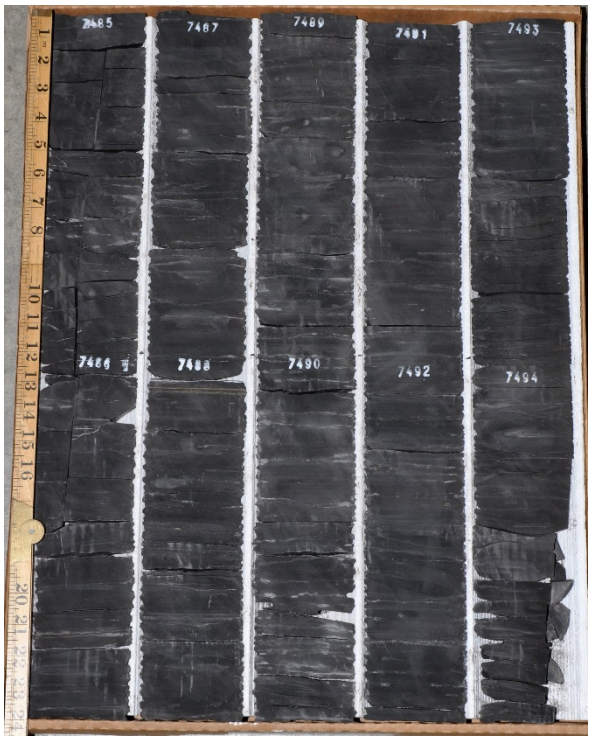

Figure 10: MIP-3H core photographs, from 7,485 to 7,495 ft.

Figure 11: MIP-3H core photographs, from 7,495 to 7,505 ft.

Figure 12: MIP-3H core photographs, from 7,505 to 7,515 ft.

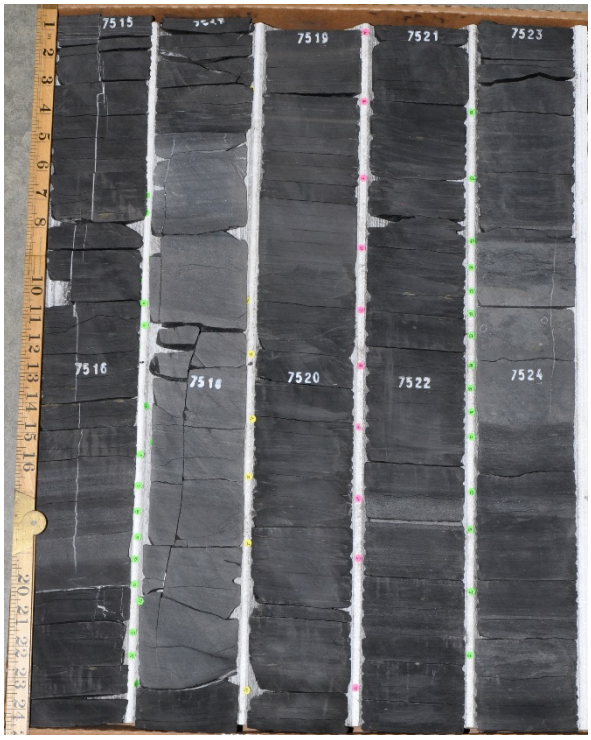

Figure 13: MIP-3H core photographs, from 7,515 to 7,525 ft.

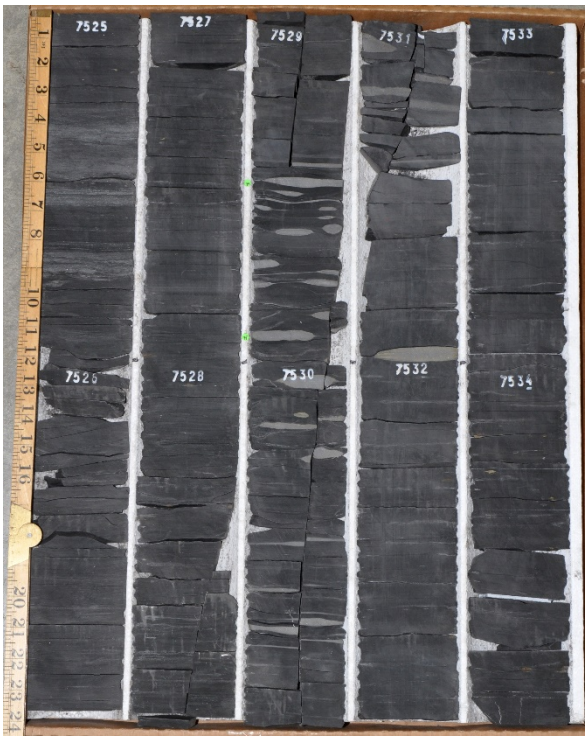

Figure 14: MIP-3H core photographs, from 7,525 to 7,535 ft.

Figure 15: MIP-3H core photographs, from 7,535 to 7,545 ft.

Figure 16: MIP-3H core photographs, from 7,545 to 7,555 ft.

Figure 17: MIP-3H core photographs, from 7,555 to 7,557 ft.

3. DATA ACQUISITION AND METHODOLOGY

The samples were evaluated using medical CT scanning, industrial CT scanning, and geophysical and geochemical core logging. Medical CT scanning and core logging were performed over the entire length of the core. Industrial CT scans, because of their time-consuming nature, were selectively conducted over regions of interest rather than the whole core.

3.1 MEDICAL CT SCANNING

The entire MSEEL MIP-3H core was scanned with a medical Toshiba® Aquilion TSX-101A/R medical scanner shown in Figure 18. The medical CT scanner generates images with a resolution in the millimeter range, with scans having voxel resolutions of 0.43 x 0.43 mm in the XY plane and 0.50 mm along the core axis. All scans were performed through the core barrels obtained in ~3 ft or smaller sections. The scans were conducted at a voltage of 135 kV and at 200 mA with a data collection diameter of 220 mm and using the helical detector rotation/acquisition. Subsequent processing and combining of stacks were performed to create 3D volumetric representations of the core and a two-dimensional (2D) cross-section through the middle of the core samples. The CT scans were exported as DICOM images by the proprietary Toshiba software and combined into 16-bit tif stacks using ImageJ (Rasband, 2017). The variation in greyscale values observed in these CT images indicates changes in the CT number obtained from the CT scans, which is directly proportional to changes in the attenuation and density of the scanned rock. Lower density regions are represented as darker greyscale values, and higher density regions are represented with brighter greyscale images.

Figure 18: Toshiba® Aquilion™ Multislice Helical Computed Tomography Scanner at the NETL used for core analysis.

3.2 INDUSTRIAL CT SCANNING

High-resolution CT scans were performed on intervals of interest using the North Star Imagining Inc. M-5000® Industrial Computed Tomography System shown in Figure 19. The system is used to obtain higher resolution scans, resolving some unclear features from the medical scans.

The scans were performed at varying voltages and currents to provide a balance between resolution and a sufficient sample penetration for each sample. Scans consisted of 1,440 radiographs, or at every 0.25°; radiographs were comprised of 10 images averaged with a 5 second acquisition for each image to ensure sufficient photon counts.

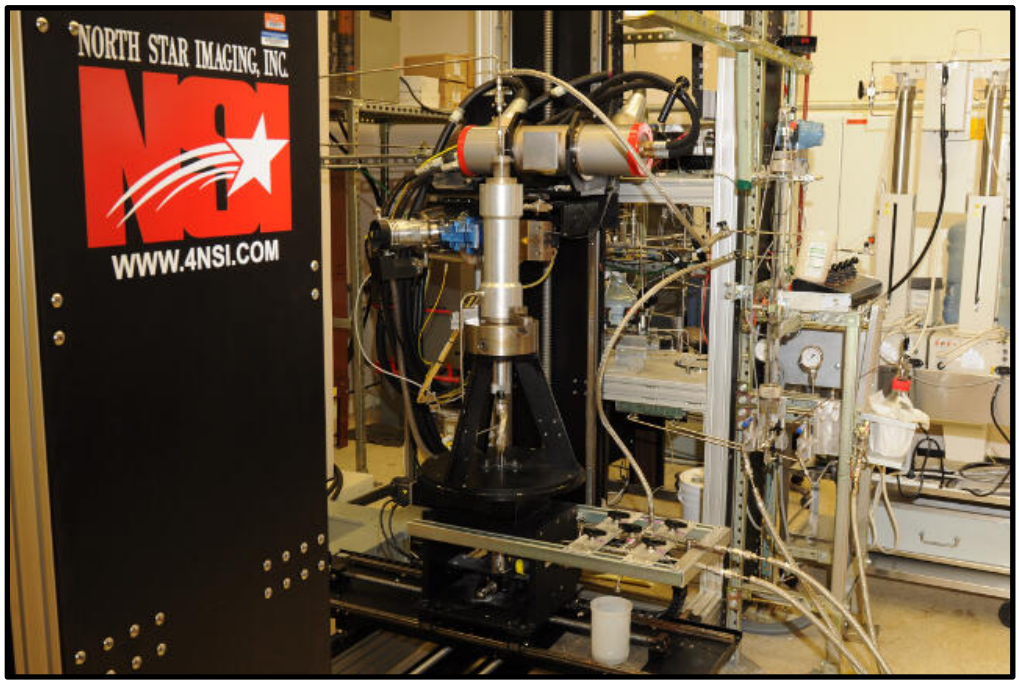

Figure 19: North Star Imaging Inc. M-5000 ® Industrial Computed Tomography Scanner at the NETL used for core analysis.

3.3 MULTI-SENSOR CORE LOGGING

Geophysical measurements of core thickness deviation, P-wave travel time, P-wave signal amplitude, magnetic susceptibility, and attenuated gamma counts were obtained with a Geotek® Multi-Sensor Core Logging (MSCL) system. Geotek® MSCL software was used to process the raw data into core thickness, P-wave velocity, gamma density, and fractional porosity values. Additionally, the system was used to measure bulk elemental chemistry with a built-in, portable X-ray fluorescence (XRF) spectrometer. The Geotek® MSCL system at NETL has many additional capabilities, however, only those that were significant to this characterization are described in the following sections.

3.3.1 P-wave Velocity

P-wave velocity measurements are performed to measure the acoustic impedance of a geologic sample with compressional waves. Acoustic impedance is a measure of how well a material transmits vibrations, which is directly proportional to density and/or material consolidation. An example of a material that has a high acoustic impedance is air, with a wave speed of 330 m/s, whereas granite has low acoustic impedance, with a wave speed of > 5,000 m/s. These measurements can be proxies for seismic reflection coefficients and can be translated to field use when doing seismic surveys.

The software associated with the MSCL measures the travel time of the pulse with a resolution of 50 ns. The absolute accuracy of the instrument measurements is ± 3 m/s with a resolution of 1.5 m/s (Geotek Ltd. Multi-Sensor Core Logger Manual, Version 05-10; Geotek Ltd., 2010).

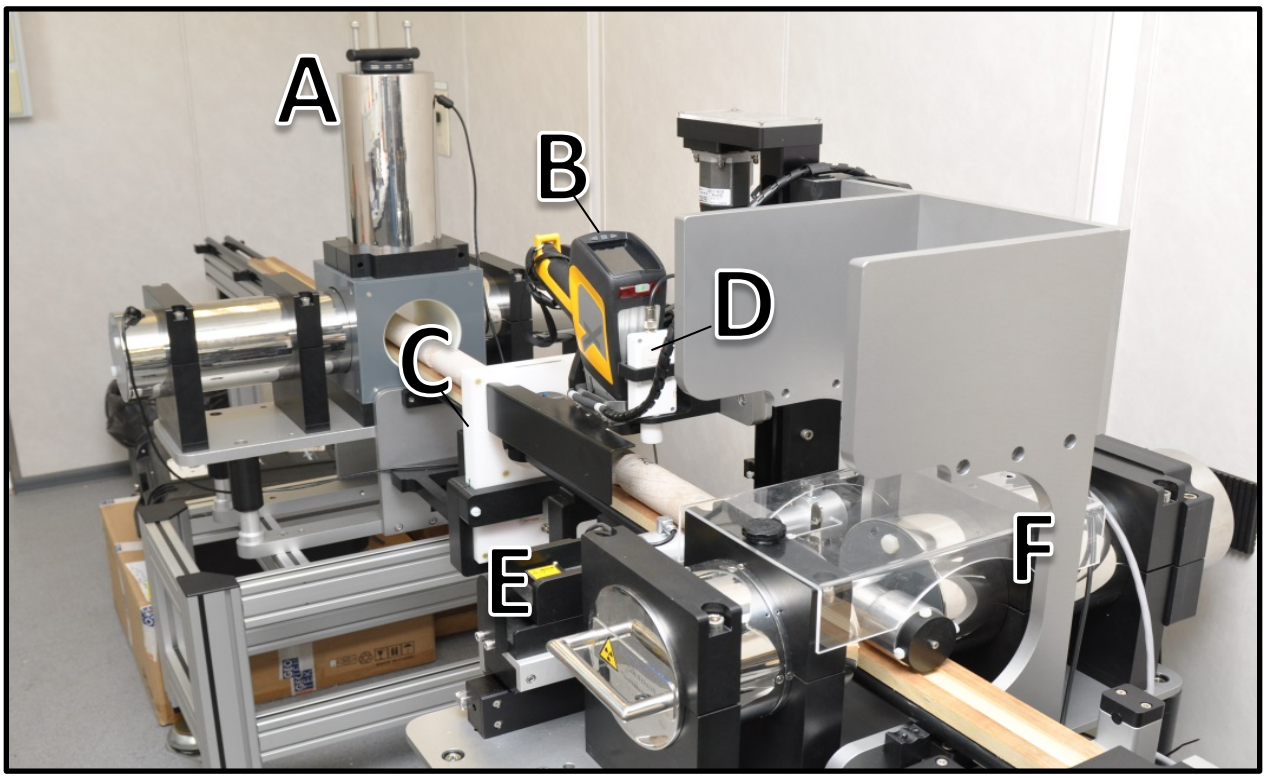

Figure 20: MSCL allows researchers to continuously run petrophysical measurements on whole core: (A) natural gamma detector; (B) X-ray fluorescence spectrometry sensor; (C) magnetic susceptibility loop sensor; (D) magnetic susceptibility point sensor; (E) P-wave velocity transducers; (F) gamma density source; and non-contacting electrical resistivity sensor (not shown).

3.3.2 Magnetic Susceptibility

Magnetic susceptibility is a measure of the degree of magnetization in the sample. Due to the split geometry of the core, the magnetic susceptibility point sensor was used. The magnetic susceptibility point sensor works by passing samples under the sensor, where an oscillator circuit produces a low intensity alternating magnetic field (~80 A/m RMS and 2 kHz) and is changed according to magnetic susceptibility of the sample. The measurement unit used is dimensionless (abbreviated simply as SI units) and is based in the original calibration, which is done via stable

iron oxides, and reference minerals which have known ranges of susceptibility (Table 2) (Geotek Ltd. Multi-Sensor Core Logger Manual, Version 05-10).

Table 2: Magnetic susceptibility values for common minerals (Modified from Geotek Ltd. Multi-Sensor Core Logger Manual, Version 05-10)

Mineral	X (*10^{-6}) SI
Water	9
Calcite	-7.5 to -39
Halite, Gypsum	-10 to -60
Illite, Montmorillonite	330 to 410
Pyrite	5 to 3,500
Hematite	500 to 40,000
Magnetite	1,000,000 to 5,700,000

3.3.3 Gamma Density

Gamma density is acquired by subjecting the sample to gamma radiation and then measuring the attenuation of that radiation. The attenuation is directly proportional to the density of the sample and is acquired by measuring the difference between radiation energy at the emission source and after it passes through the sample. Specifically, the MSCL software calculates the bulk density, ρ, by using the following equation:

$$\rho = \left(\frac{1}{\mu d}\right) \ln\left(\frac{I_o}{I}\right)$$

Where μ = Compton attenuation coefficient, d = thickness, I_o = source intensity, and I = measured intensity.

3.3.4 X-ray Fluorescence Spectrometry

In addition to the geophysical measurements a portable handheld Innov-X® X-Ray Fluorescence Spectrometer was used to measure relative elemental abundances. Three suites were measured from the handheld XRF (hhXRF) tool: Mining-Plus Suite, Mining Suite, and Soil Suite. The Mining and Soil Suites were run at a 2 cm resolution at 20 seconds per beam exposure time, over the entire cored section (7,445 to 7,557 ft). The Mining-Plus Suite was run at a 2 cm resolution at 60 seconds per beam exposure time over a 38 ft section in the lower Marcellus (7,517 to 7,555 ft).

The Mining Suite determines primarily major elements (Mg, Al, Si, P, S, Cl, Fe, K, Ca, and Ti) with some minor elements (V, Cu, Ni, and Pb) and an aggregated “light element” (H to Na). The Soil Suite utilizes a 3-beam analysis that resolves primarily major elements (P, S, Cl, Ca, K, Fe, and Ti), minor elements (V, Cr, Mn, Fe, Co, Ni, Cu, and Zn), trace elements (Rb, Sr, Y, Zr, Nb, Mo, Ag, Cd, Sn, Sb, Cs, Ba, Th, U, W, Hg, Pb, and Bi), and an aggregated “light element” (H to

Si). The Mining-Plus Suite utilizes a 2-beam analysis that resolves primarily major elements (Mg, Al, Si, P, S, Cl, Fe, K, Ca, and Ti), minor elements (V, Cu, Ni, Cr, Mn, and Pb), trace elements (Co, Zn, As, Zr, Mo, Ag, Cd, Sn, Sb, Hf, W, and Bi), and an aggregated "light element" (H to Na) (Figure 21). All three suites resolve elemental abundances that are reported relative to the total elemental composition, i.e. out of 100% weight.

The XRF spectrometer measures elemental abundances by subjecting the sample to X-ray photons. The high energy of the photons displaces inner orbital electrons in the respective elements. The vacancies in the lower orbitals cause outer orbital electrons to "fall" into lower orbits to satisfy the disturbed electron configuration. The substitution into lower orbitals causes a release of a secondary X-ray photon, which has an energy associated with a specific element. These relative and element specific energy emissions can then be used to determine bulk elemental composition.

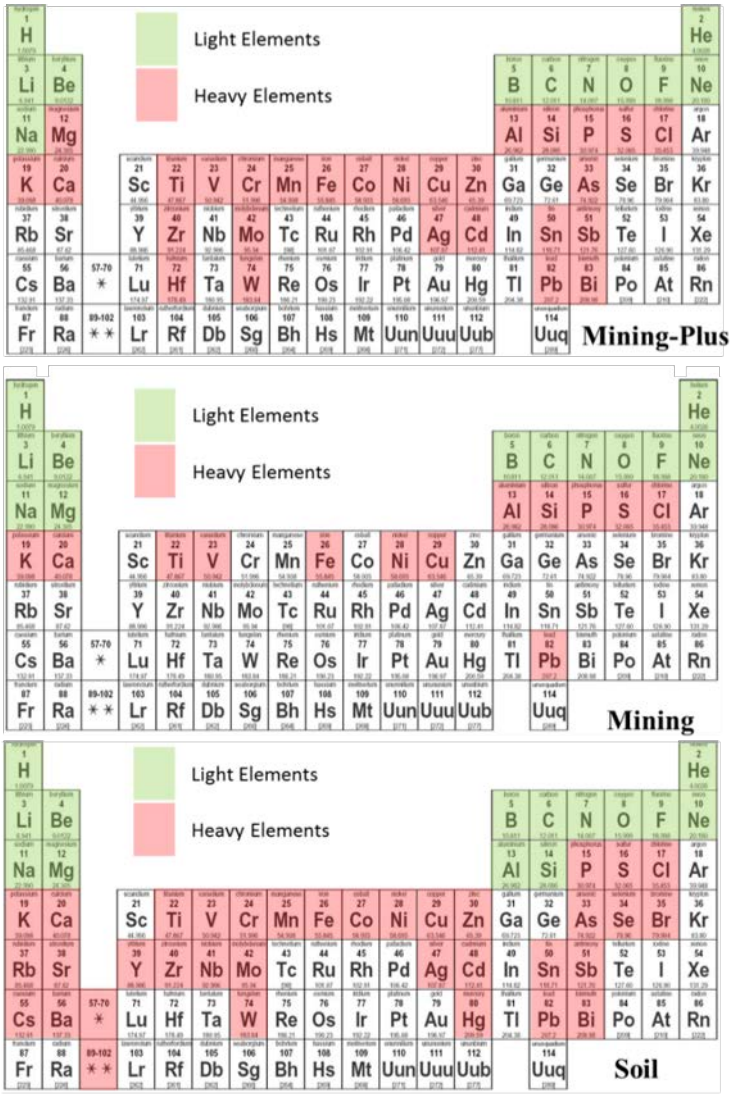

Figure 21: Periodic table showing elements measurable for each suite (Mining-Plus, Mining, and Soil) by the Innov-X® X-Ray Fluorescence Spectrometer.

In addition to the handheld XRF measurements, 68 powdered samples were analyzed using traditional methods by Hamilton University using a Thermo ARL Preform'X spectrometer with approximately 2 hours of exposure time (Hupp, 2017). For this study, these are referred to as "Hamilton Suite" samples. The Hamilton Suite includes major, minor, and trace elements. The Hamilton Suite has high accuracy to standards (Figure 22); and therefore, is used to evaluate the reliability and accuracy of the handheld XRF suites.

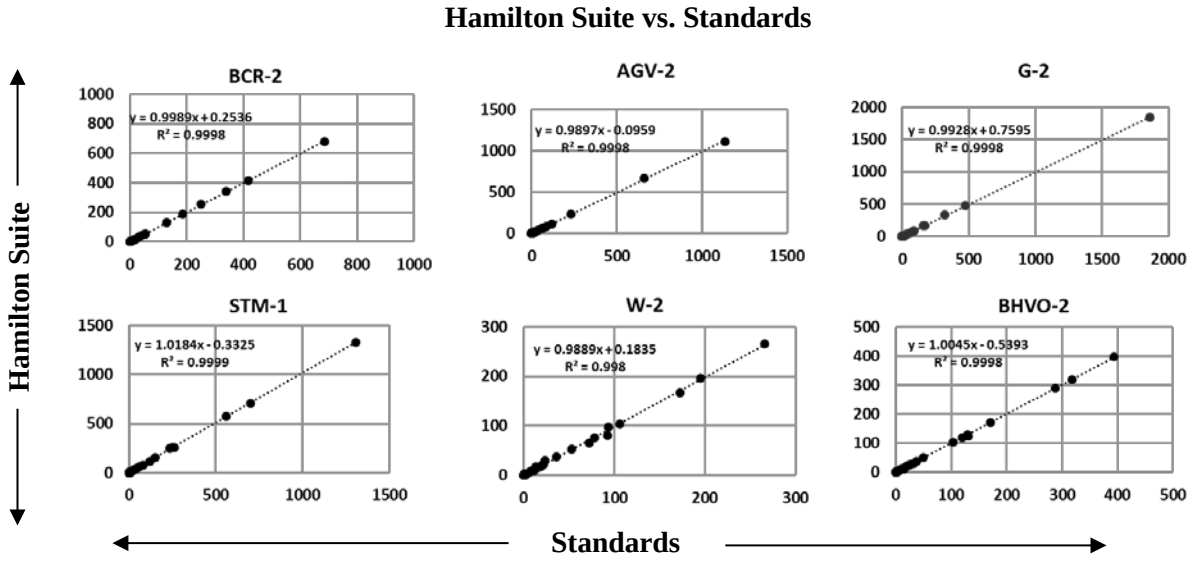

Figure 22:The six crossplots above represent the standards ran in the Hamilton Suite. Hamilton values plotted along the x-axis and the standards values are measured along the y-axis. All elements are displayed in the x-plots above.

Figure 23 represents the correlations between all similar elements between the Hamilton Suite and handheld suites. All handheld suites were corrected for errors exceeding 2% of the measurement prior to calculation of correlation coefficients. Some elements, such as, phosphorous and magnesium are below the detection limits and are not included in the calculations. The poor correlation for sulfur is due to loss on fusion of the powdered samples in the Hamilton Suite (Hupp and Donovan, 2018). In general, major and some minor elements have moderate/strong correlation compared to the Hamilton Suite. Exposure time also affects the correlation between the handheld and the Hamilton Suite. Longer exposure times with all scanning suites of the Innov-X® X-Ray Fluorescence Spectrometer resulted in better correlations with the Hamilton Suite, specifically in trace elements.

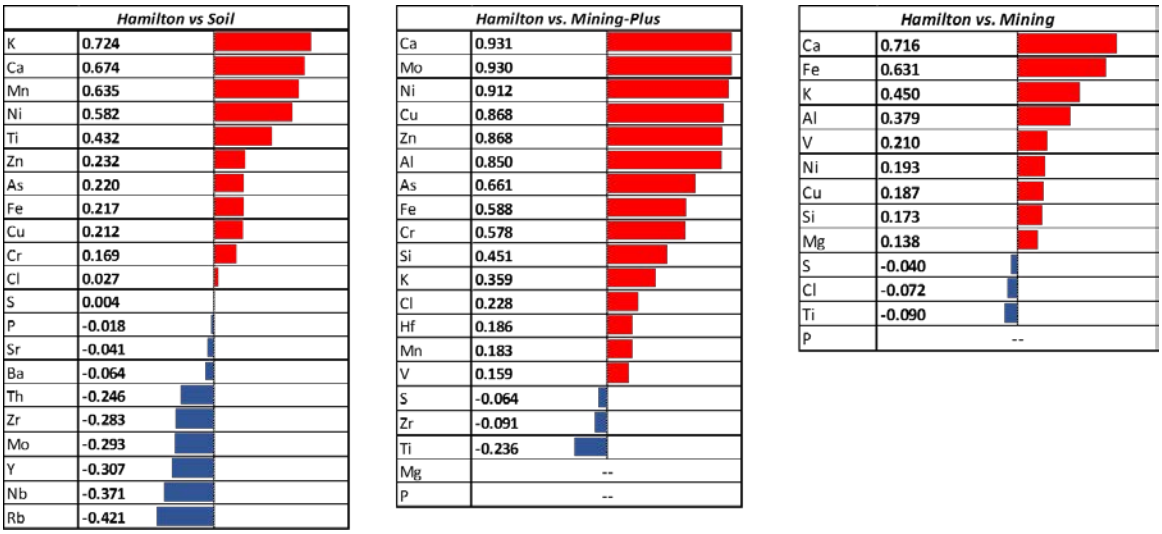

Figure 23: Correlation between hhXRF Suites and Hamilton Suite, red bars indicate positive correlation (0-1) and blue indicates negative correlations (-1-0).

3.4 SOURCE ROCK ANALYSIS

Pyrolysis experiments were performed by NETL researcher, Chloe Wonnell, using the Weatherford Source Rock Analyzer. A total 47 samples from the MIP-3H well were taken at intervals of approximately 3 ft (1 m) with 5 repeat samples to confirm accuracy. The pyrolysis dataset includes: *TOC*- total organic carbon; *s1*- amount of free hydrocarbons; *s2*- amount of hydrocarbons generated through the heating of nonvolatile organic matter; *s3*- CO_2 released during the pyrolysis experiment; *cTemp* (Tmax)- temperature at the max release of organic matter; *HI*- hydrogen index; *OI*- oxygen index; *PI*- production index; *s1/TOC*- oil and contamination index for samples; and *tTemp*- the maximum temperature reached during the pyrolysis experiment. For more details on the Weatherford Source Rock Analyzer see Wonnell (2015). This dataset is available on NETL's Energy Data eXchange (EDX) online system using the following link: https://edx.netl.doe.gov/dataset/MIP3H-Scans.

4. RESULTS

The following section contains the data obtained from the medical CT, the industrial CT, and the MSCL scans of the core obtained from MSEEL MIP-3H well.

4.1 MEDICAL CT SCANS

Processed 2D slices of the medical CT scans through the cores are shown first, followed by various analyses of fractures and variations in the shale structure observed from the medical CT scans. As previously discussed, the variation in greyscale observed in the medical CT images indicate changes in the CT number obtained, which is directly proportional to changes in the attenuation and density of the scanned rock. Darker regions are less dense zones with lower X-ray attenuation (e.g. gas filled fractures) and lighter regions are more dense zones with higher X-ray attenuation. Very highly attenuating materials within the core (e.g. pyrite nodules) resulted in streaking CT artifacts (Cnudde and Boone, 2013) which are visible in the following images as white/bright rays emanating from the rock (e.g. Figure 29 and Figure 34).

4.1.1 XZ Planes

A 2D image through the center of each retrieved core barrel can be found in Figure 25 through Figure 32. These are referred to as "XZ" planes with the coordinates that are shown in Figure 24. There is no scale bar shown in these images; the retrieved core has a diameter of 4 in. (10.16 cm) for reference. The labels below each 2D XZ plane in Figure 25 through Figure 32 are the depth at the bottom of each core; the full range of core lengths shown in each figure is listed in the figure captions. The greyscale values were shifted in these images to best represent the structure of the core in each image.

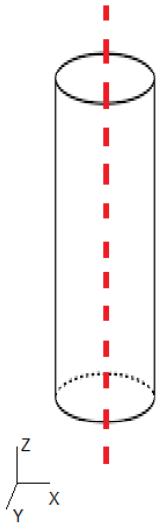

Figure 24: Schematic of the XZ isolated plane through the vertical center of the medical CT scans of the MSEEL MIP-3H core

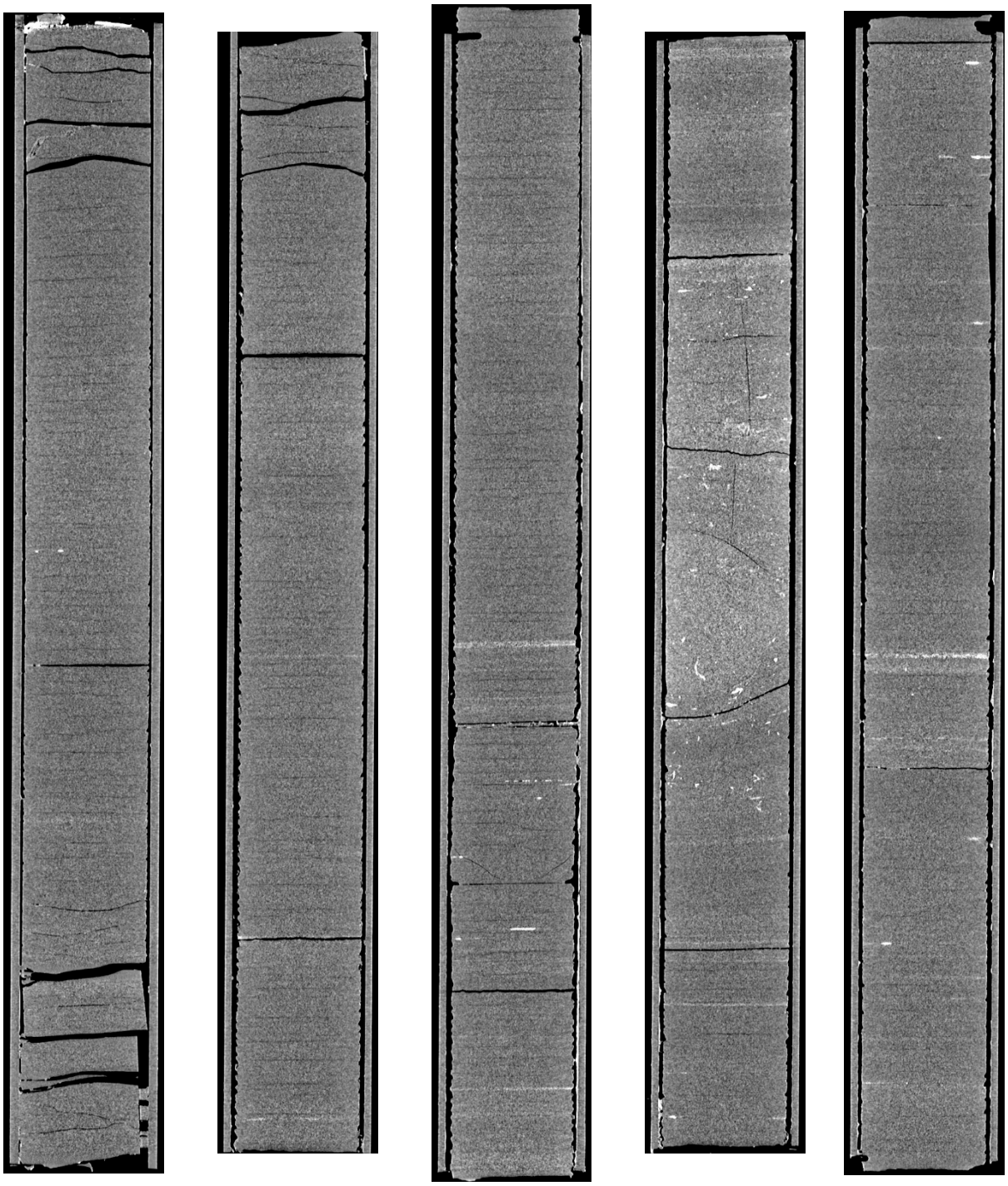

7,442–7,445 ft **7,445–7,448 ft** **7,448–7,451 ft** **7,451–7,454 ft** **7,454–7,457 ft**

Figure 25: 2D isolated planes through the vertical center of the medical CT scans of the MSEEL MIP-3H core from 7,442 to 7,457 ft.

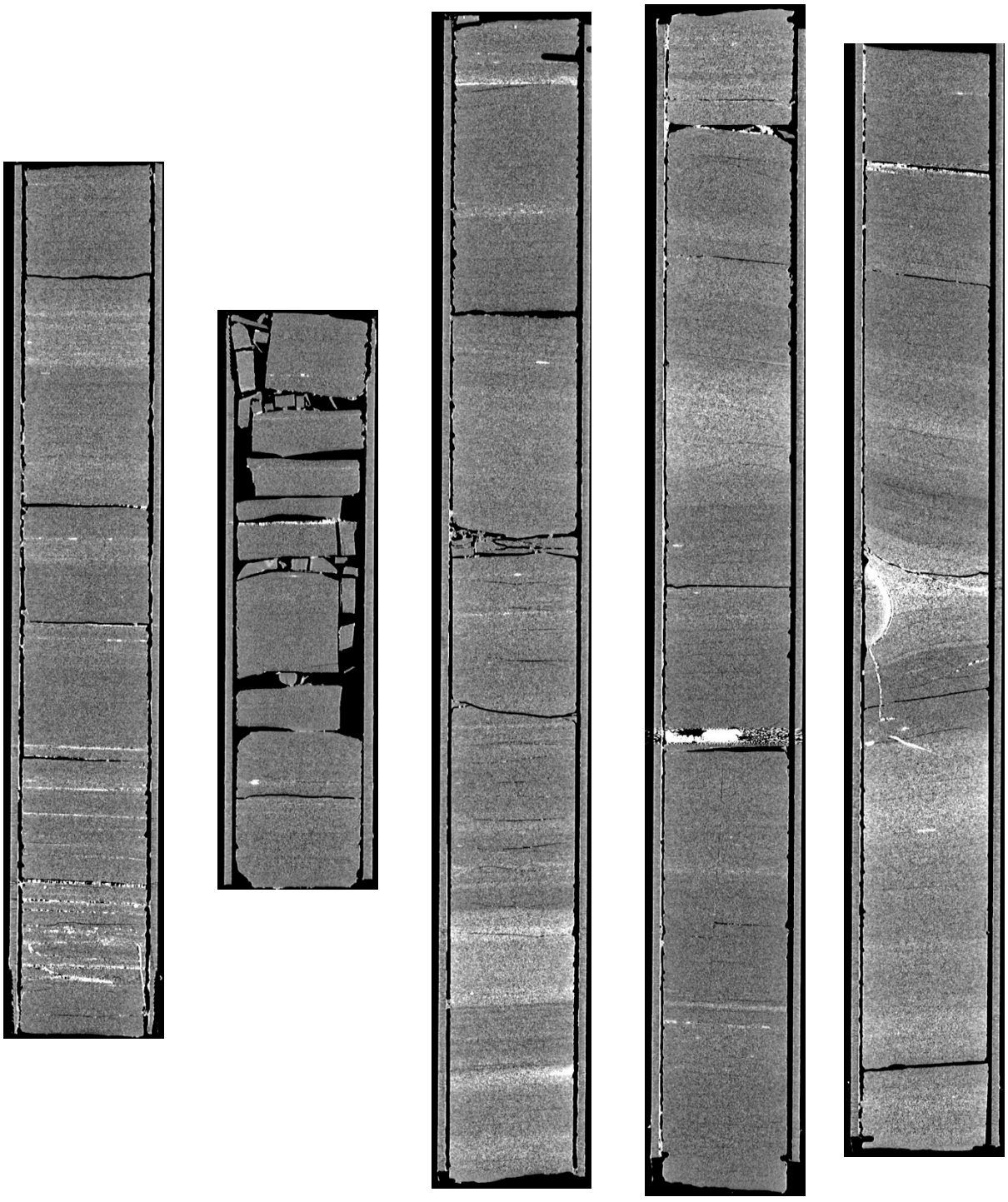

7,457–7,460 ft **7,460–7,462 ft** **7,462–7,464 ft** **7,464–7,467 ft** **7,467–7,470 ft**

Figure 26: 2D isolated planes through the vertical center of the medical CT scans of the MSEEL MIP-3H core from 7,457 to 7,470 ft.

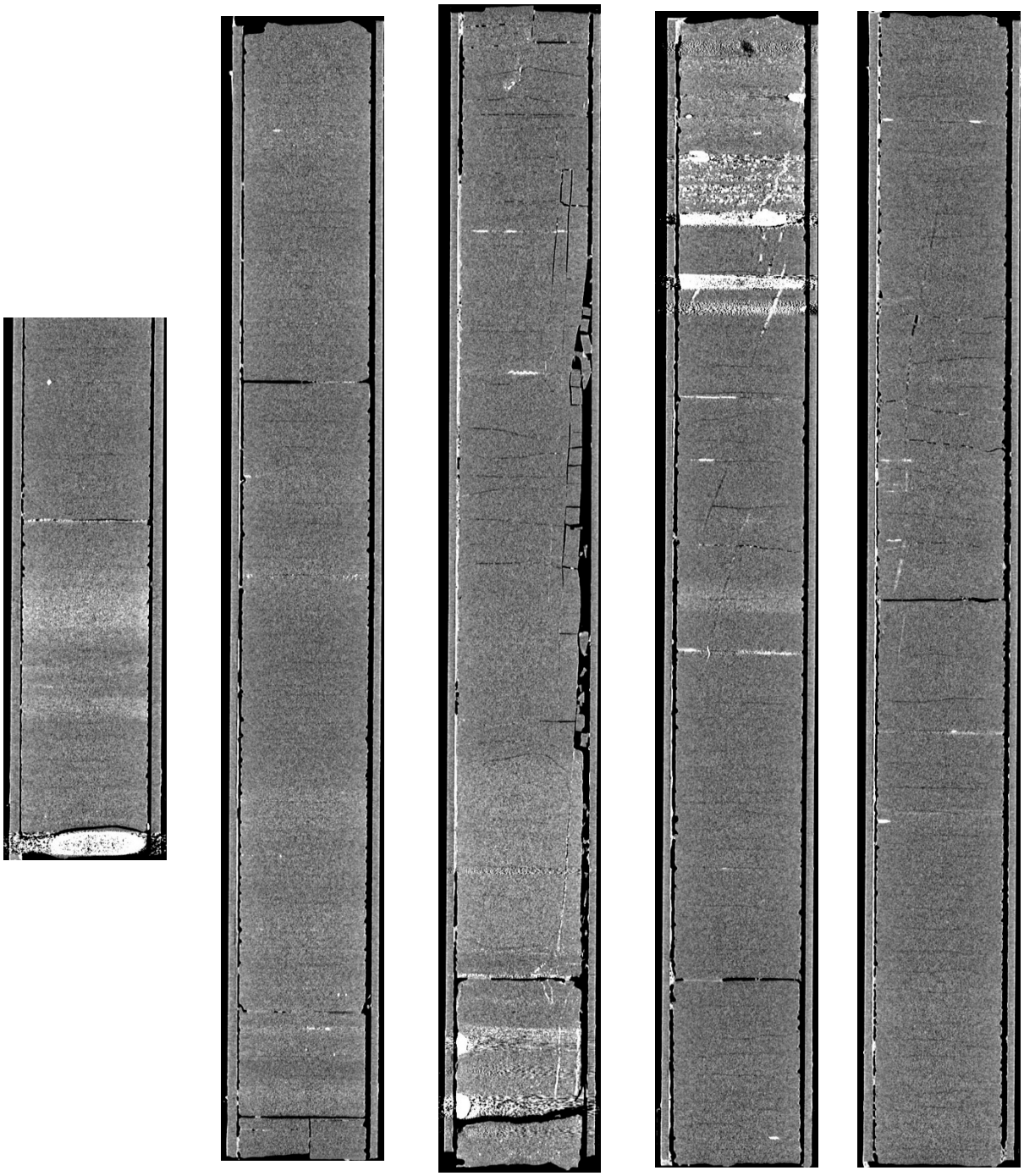

7,470–7,473 ft **7,473–7,476 ft** **7,476–7,479 ft** **7,479–7,482 ft** **7,482–7,485 ft**

Figure 27: 2D isolated planes through the vertical center of the medical CT scans of the MSEEL MIP-3H core from 7,470 to 7,485 ft.

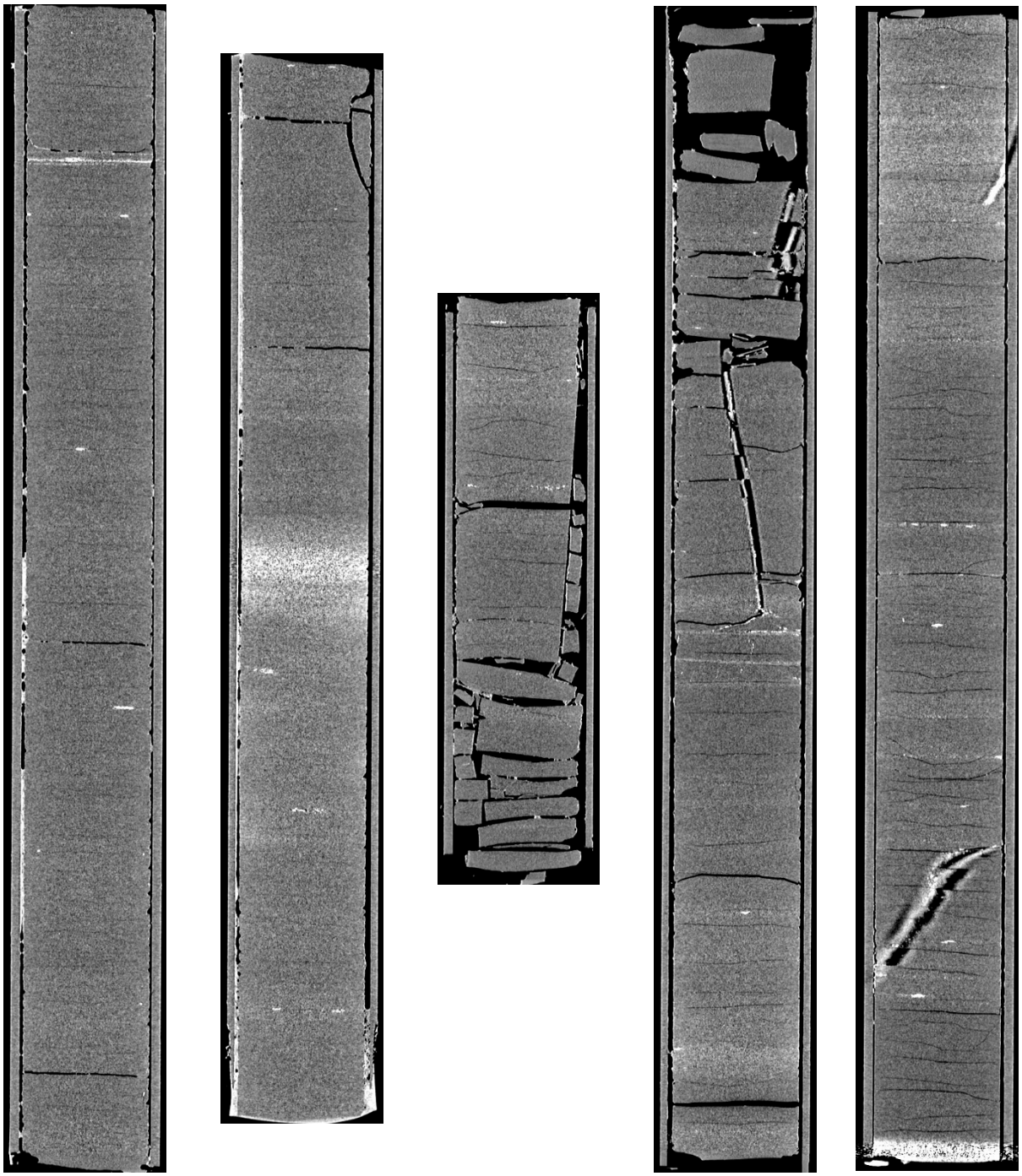

7,485–7,488 ft **7,488–7,491 ft** **7,491–7,493.25 ft** **7,493.25–7,495 ft** **7,495–7,498 ft**

Figure 28: 2D isolated planes through the vertical center of the medical CT scans of the MSEEL MIP-3H core from 7,485 to 7,498 ft.

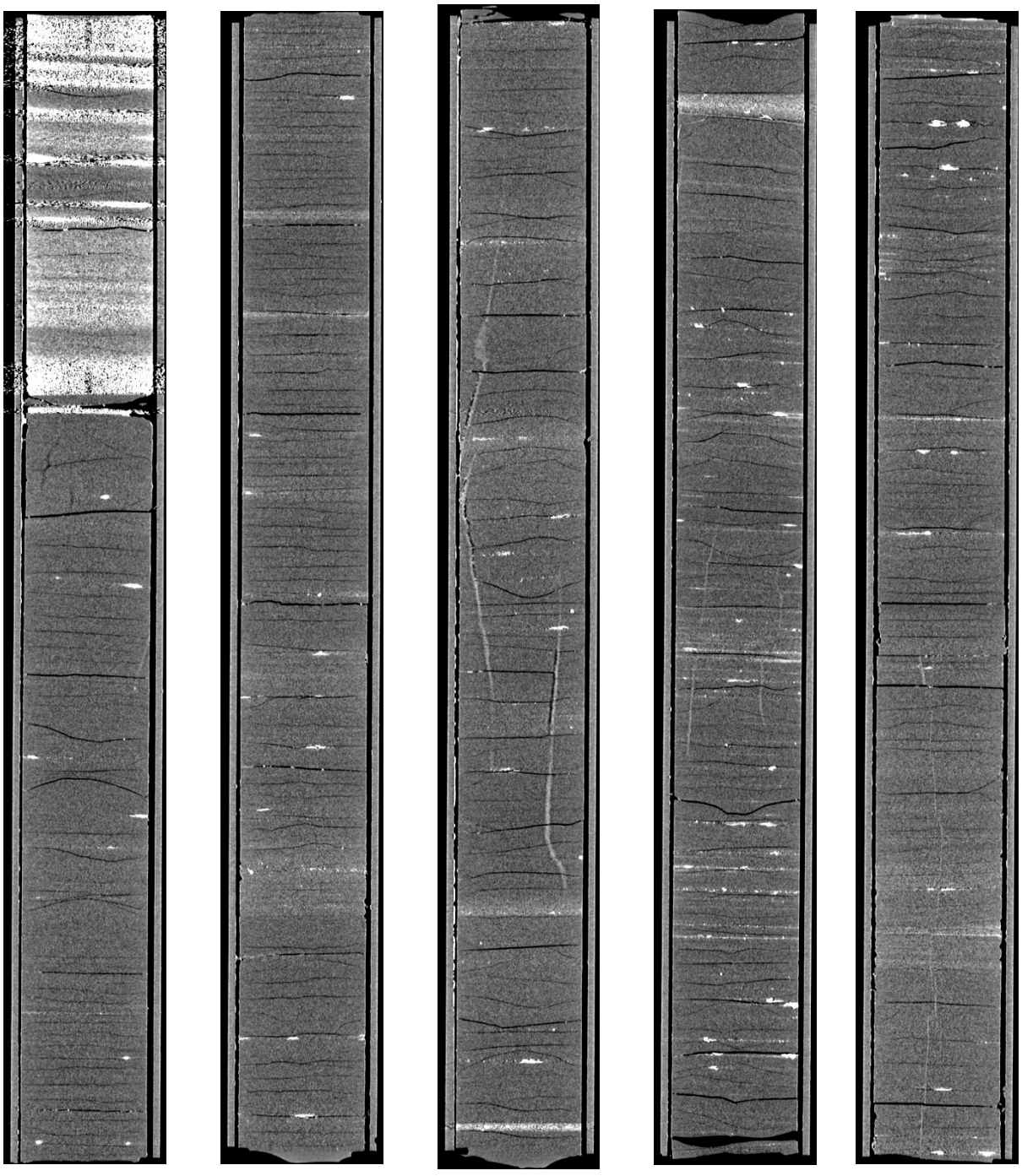

7,498–7,501 ft **7,501–7,504 ft** **7,504–7,507 ft** **7,507–7,510 ft** **7,510–7,513 ft**

Figure 29: 2D isolated planes through the vertical center of the medical CT scans of the MSEEL MIP-3H core from 7,498 to 7,513 ft.

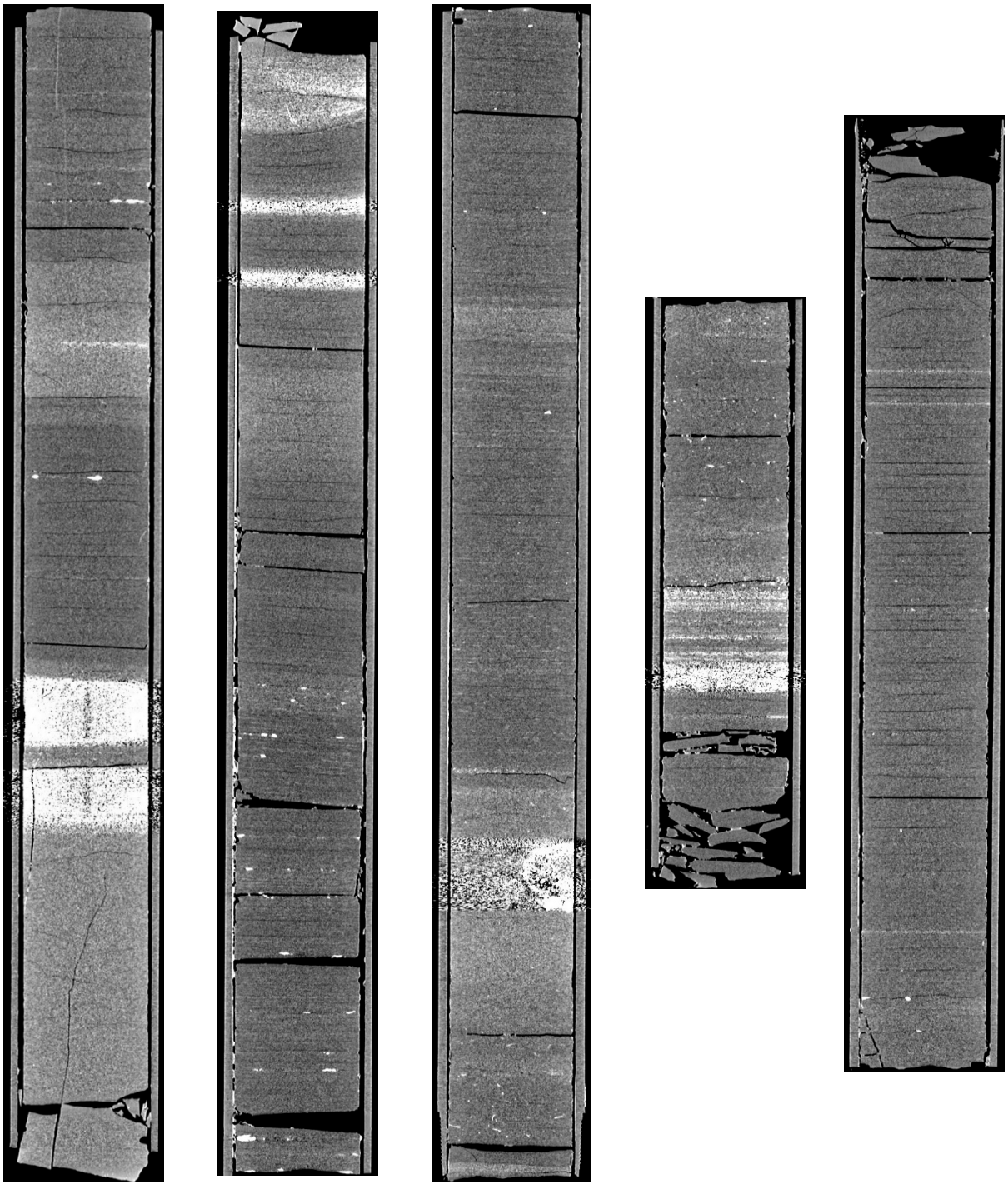

7,513–7,516 ft **7,516–7,519 ft** **7,519–7,522 ft** **7,522–7,525 ft** **7,525–7,526.5 ft**

Figure 30: 2D isolated planes through the vertical center of the medical CT scans of the MSEEL MIP-3H core from 7,513 to 7,526.5 ft.

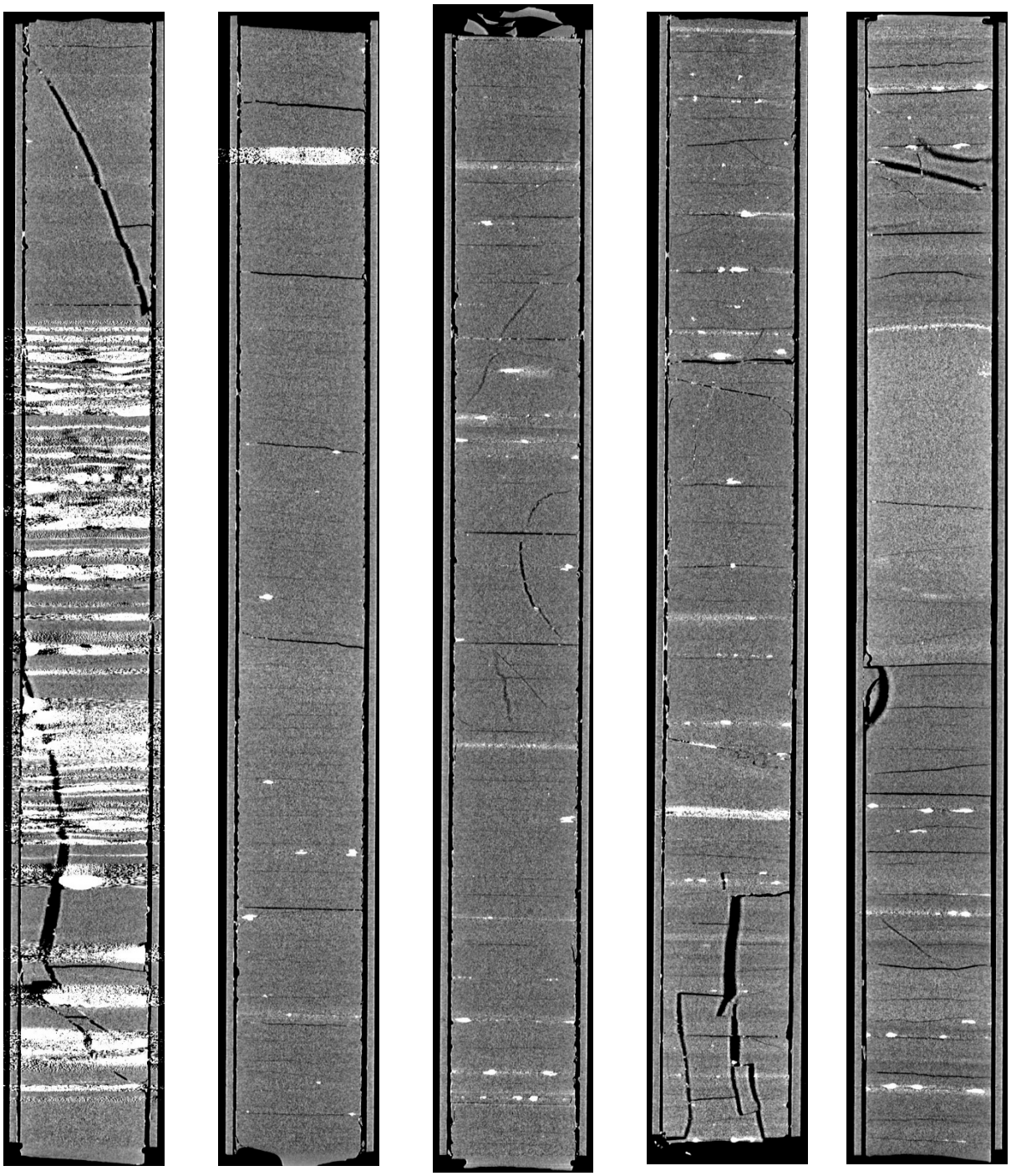

7,526.5–7,529 ft **7,529–7,532 ft** **7,532–7,535 ft** **7,535–7,538 ft** **7,538–7,541 ft**

Figure 31: 2D isolated planes through the vertical center of the medical CT scans of the MSEEL MIP-3H core from 7,526.5 to 7,541 ft.

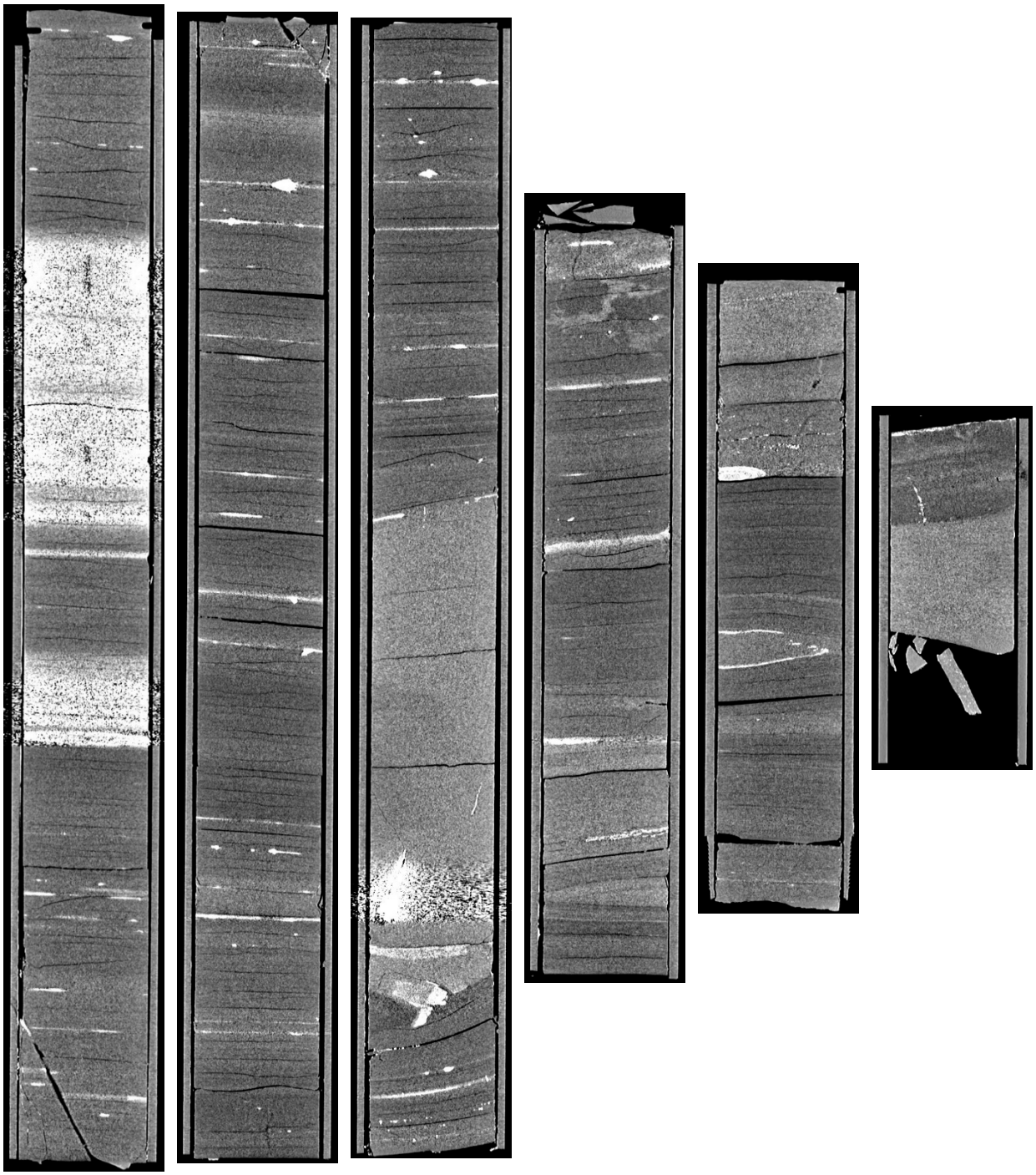

7,541–7,544 ft **7,544–7,547 ft** **7,547–7,550 ft** **7,550–7,553 ft** **7,553–7,555 ft** **7,555–7,557 ft**

Figure 32: 2D isolated planes through the vertical center of the medical CT scans of the MSEEL MIP-3H core from 7,541 to 7,557 ft.

4.1.2 XY Planes

Two-dimensional images along the length of each retrieved core barrel are available on NETL's EDX using the following link: https://edx.netl.doe.gov/dataset/MIP3H-Scans. These are referred to as “XY” planes with the coordinates that are shown in Figure 33. The distance between adjacent images is 1.5 in. (3.8 cm), which enabled 25 slices to be shown for full 3-ft-long cores; shorter core barrels have fewer images associated with them. There is no scale bar shown in these images; the retrieved core had a diameter of 4 in. (10.16 cm) for reference. The greyscale values were shifted in these images to best illustrate the structure along the length of the core in each image. Examples are shown in Figure 34 and Figure 35.

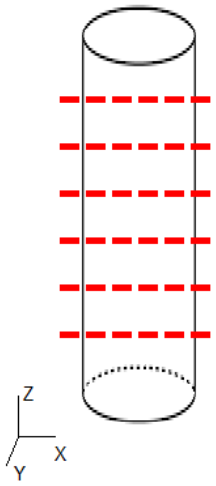

Figure 33: Schematic of the XY isolated planes through the medical CT scans of the MSEEL MIP-3H core.

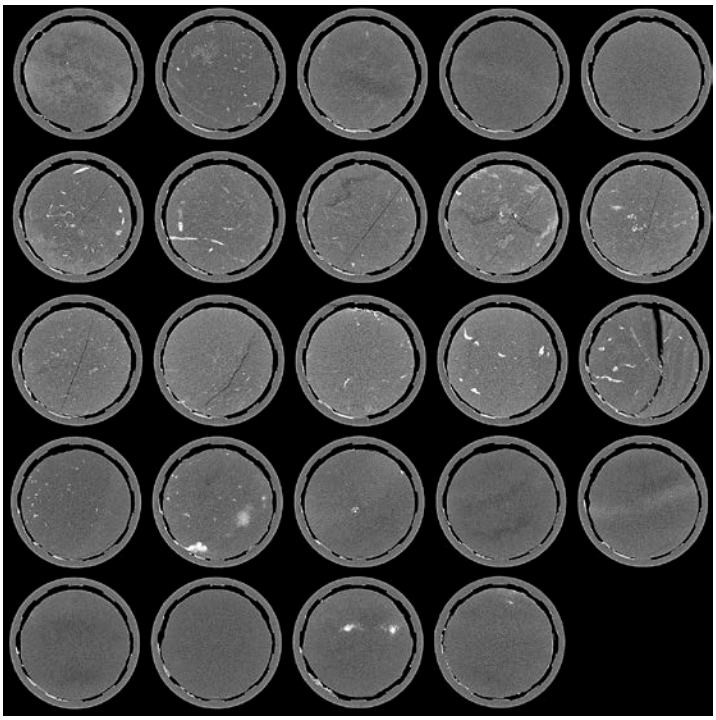

Figure 34: 2D isolated images through the cross-sectional horizontal planes of the medical CT scan of the MSEEL MIP-3H core from 7,451 to 7,454 ft.

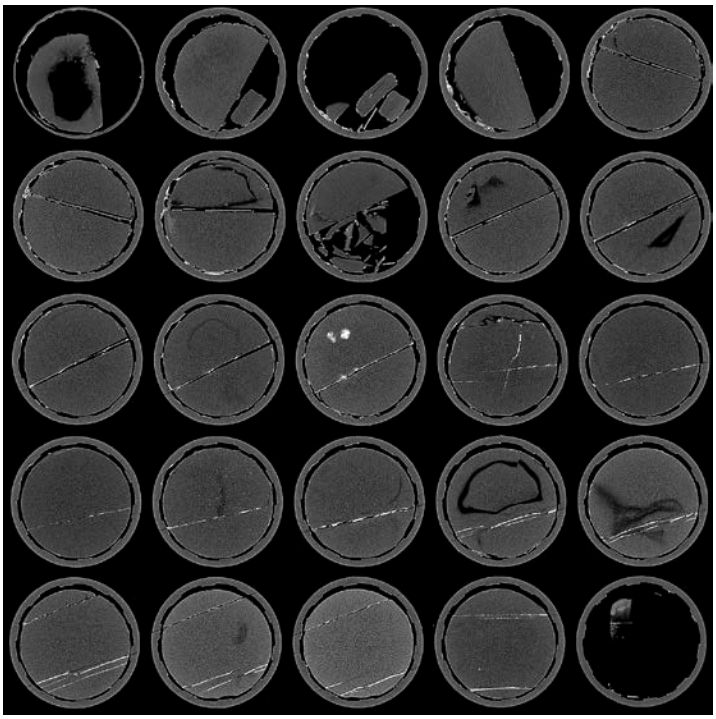

Figure 35: 2D isolated images through the cross-sectional horizontal planes of the medical CT scan of the MSEEL MIP-3H core from 7,493.25 to 7,495 ft.

4.2 INDUSTRIAL CT SCANS

The industrial CT scans were conducted for MIP-3H samples at a resolution of 61.5 µm and the MIP-SW sidewall cores at 25.2 µm. The greyscale values in the following images were used to isolate and visually differentiate objects of interest in the scans, in the example provided pyrite nodules, using the interactive learning and segmentation toolkit ilastik (Sommer et al., 2011). Figure 36 shows the resolution difference between the medical (430 µm x 430 µm x 500 µm) and industrial CT scans (61.5 µm)^3. Both scans were produced with the core in the original core barrels, prior to cutting the core into 1/3 and 2/3 sections. The increased resolution decreases the amount of attenuation "shadowing" of high-density features and allows us to have a better understanding of the geometry of these features.

The premise of isolating features is to first segment out the feature based on its unique greyscale value. Once this isolation has occurred, the next steps are to differentiate multiple isolated features and then combine them into one coherent visual representation. Figure 37 shows these feature isolations to enhance the ability of the reader to discern differences observed in the MIP-SW core. This example isolated the pyrite and other high-density minerals from the matrix. Due to the time-intensive nature of the industrial CT scans (2 hours or more), only select intervals were scanned. Raw CT images are available for additional analysis on NETL's EDX using the following link: https://edx.netl.doe.gov/dataset/MIP3H-Scans.

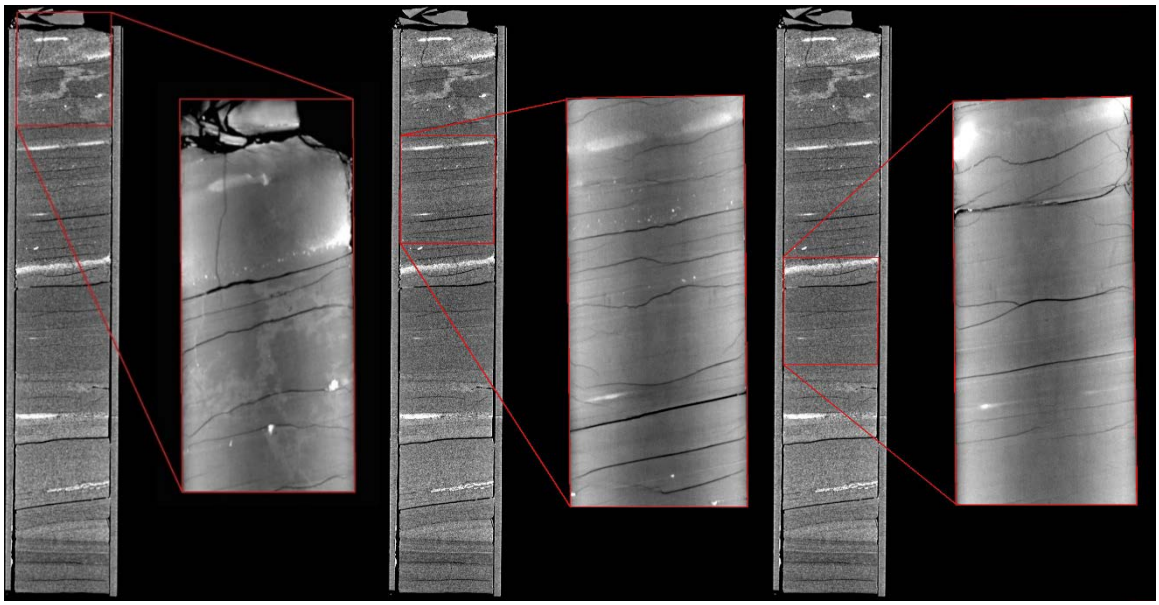

Figure 36: Medical CT scan (on left) from 7,553 to 7,555 ft and the corresponding industrial CT scans (on right) from 7,553 to 7,554.6 ft (in descending order left to right).

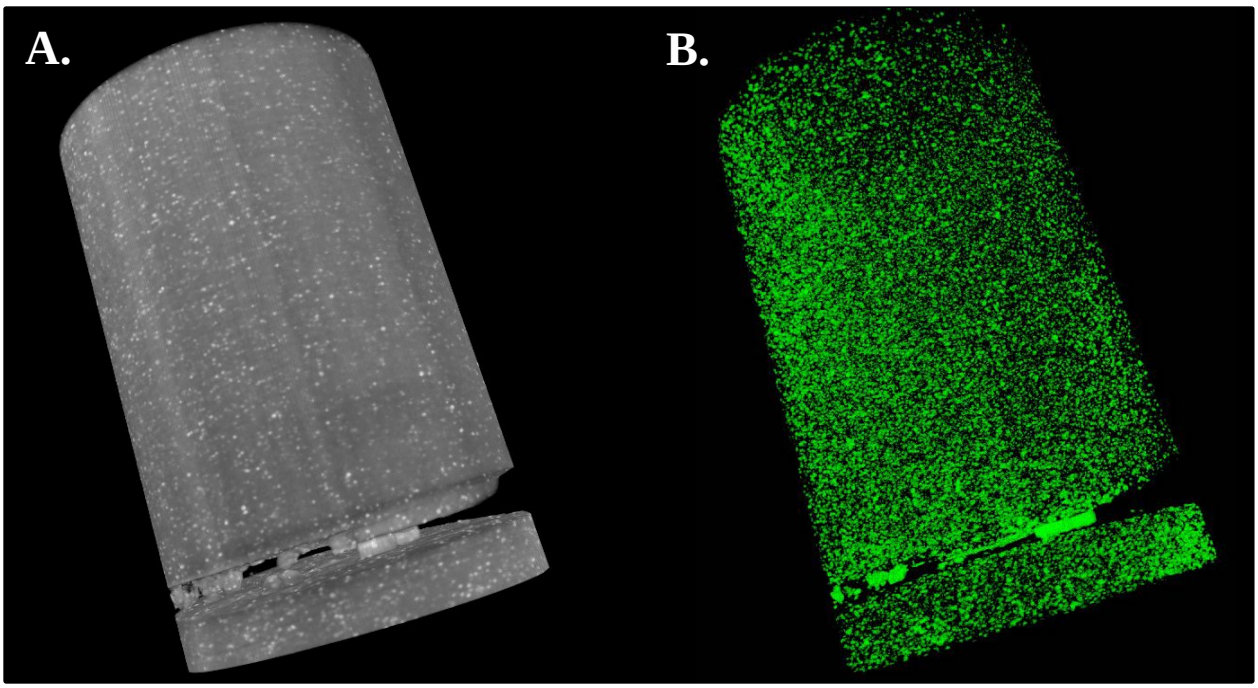

Figure 37: Visualization of features from MIP-SW sidewall core at 7,425 ft. (A) 3D volumetric CT scan (B) 3D volumetric CT scan with pyrite and other high-density minerals isolated.

4.3 MSCL CORELOGGER AND PYROLYSIS

The compiled core logs were scaled to fit on single pages for rapid review of the combined data from the medical CT scans, pyrolysis, XRF, and MSCL measurements. A series of seven core logs were made to display the results. Figure 38 displays the geophysical measurements from the MSCL core logger with lithology logs and medical CT scan images. Figure 39 to Figure 41, show the four most abundant elements (three for Mining-Plus), remaining elements, and a relative distribution of elements for the whole well. Figure 44 to Figure 46, displays total organic carbon (TOC) from pyrolysis, calculated ratios from the XRF data for each suite, and combined medical CT-scan images. Features that can be derived from these combined analyses include determination of mineral locations, such as pyrite, from magnetic susceptibility and using the XRF to inform geochemical composition and mineral form.

Data from the MSCL that was obtained with P-wave velocity less than 330 m/s has been removed from these logs. This low P-wave velocity is less than the anticipated velocity through air, indicating a highly fractured zone and unreliable readings. The location of these fractured zones was confirmed through visual examination and with the medical CT scanned images.

The elemental results are displayed with the four top elemental proportions and the remaining elemental proportions in percent for each suite. These include light elements (sodium and lighter), chlorine, calcium, and silicon for Mining Suite (Figure 39), light elements (silicon and lighter), calcium, sulfur, and iron for Soil Suite (Figure 40); and light elements (sodium and lighter), calcium, and silicon for Mining-Plus Suite (Figure 41). Additionally, pie charts of Figure 42 and Figure 43 show the relative proportions of all elements in suites; in the case of Mining-Plus and Soil Suites secondary pie charts represent 0.3% and 0.75% of the whole, respectively.

Trends in elemental ratios can provide insight into mineral composition, oxidation state, and depositional setting. Examples include: Ca/Si and Ca/K, which provides information on relative abundance of calcium carbonates versus silicates and clays, respectively; Ti/Al, which provides information about terrigenous input; Si/Al, which provides information on the abundance of illite and micas versus other clays; Mn/Fe, provides information on oxidation, where a decrease in the ratio is related to zones of anoxic/euxinic conditions and an increase is related to zones of dysoxic/oxic conditions; S/Fe, which provides information on the abundance of pyrite versus Fe oxide minerals. Additionally, magnetic susceptibility can test for iron sulfides (reducing) or oxidized Fe and sulfate. Pyrite (reduced) should have low magnetic susceptibility. Fe oxide or hydroxide should have high magnetic susceptibility. Natural gamma is a proxy for organic carbon as well. These broad trends can quickly give information on large suites of core and direct more focused research. These logs are presented in the following images: Figure 38, Figure 44, Figure 45, and Figure 46.

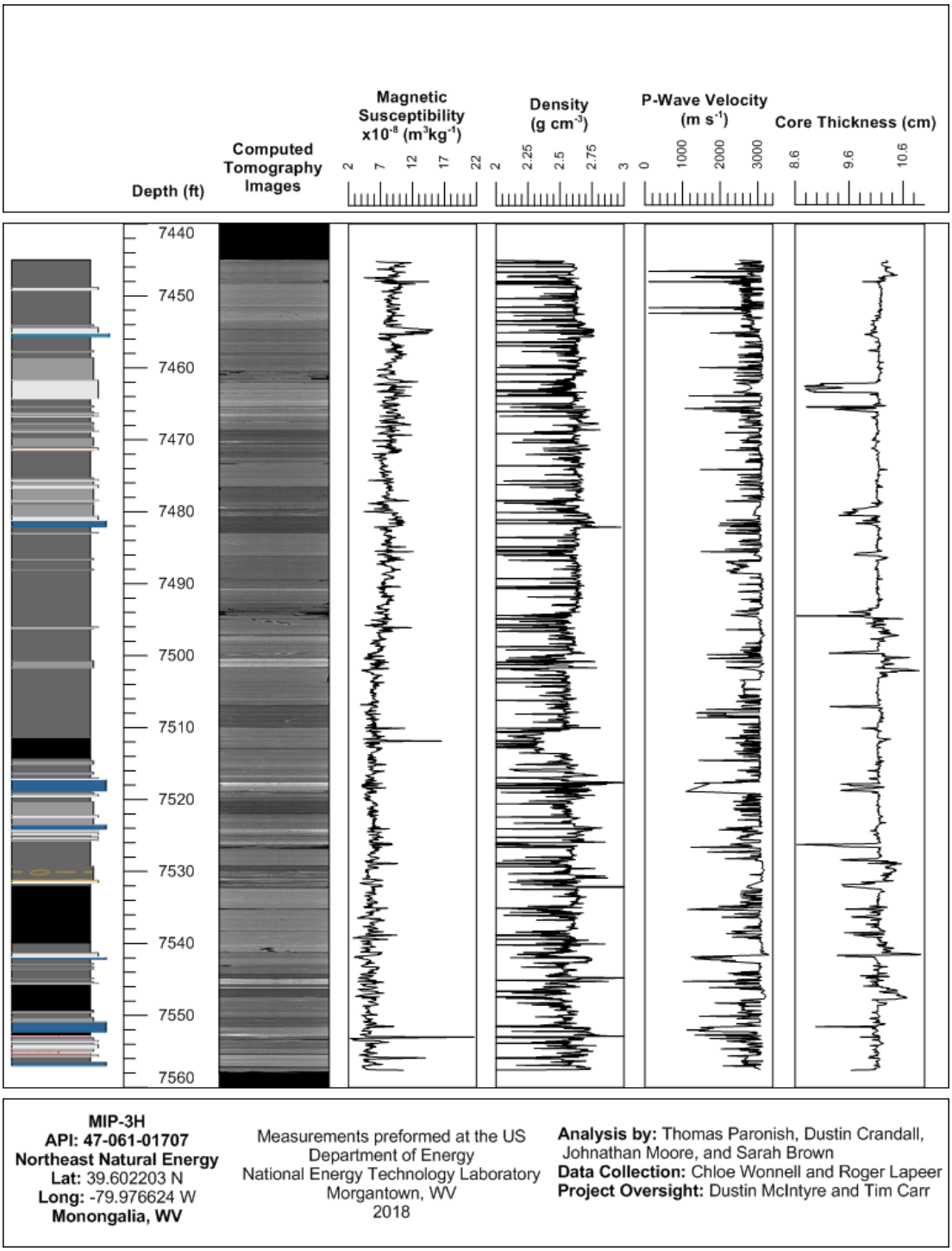

Figure 38: Compiled core log detailing the MSCL core logger geophysical measurements; column 1: Strat. column (see Figure 5 for lithology key), 2: CT Images, 3: Magnetic Susceptibility ($x10^{-8}$ ($m^3 kg^{-1}$)), 4: Gamma Density (g cm^{-3}), 5: P-wave Velocity (m s^{-1}), and 6: Core Thickness (cm).

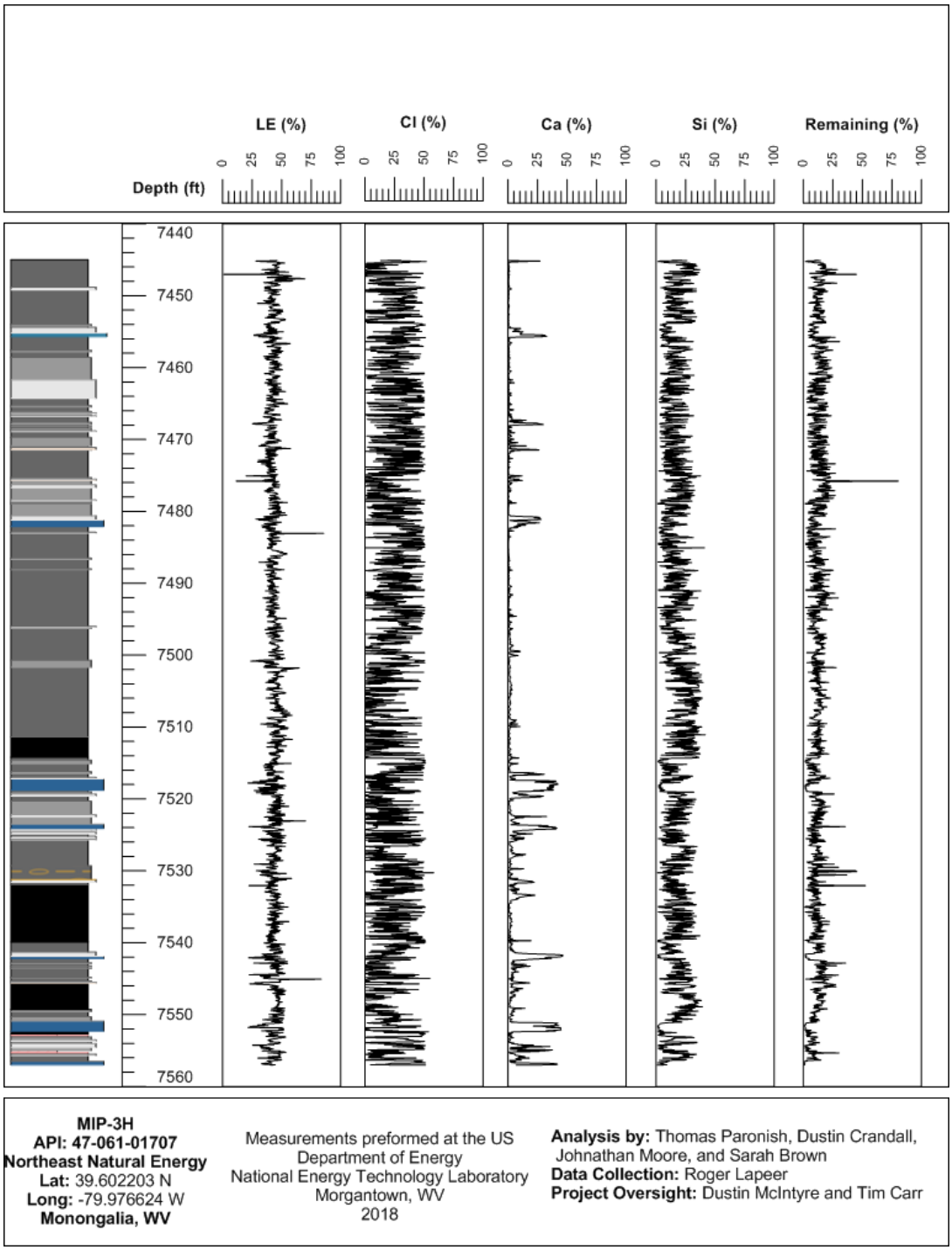

Figure 39: Compiled core log detailing the Mining Suite elemental results; column 1: Strat. column (see Figure 5 for lithology key), 2: light elements (LE) (%), 3: chlorine (Cl) (%), 4: calcium (Ca) (%), 5: silicon (Si) (%), and 6: remaining elements contribution (%).

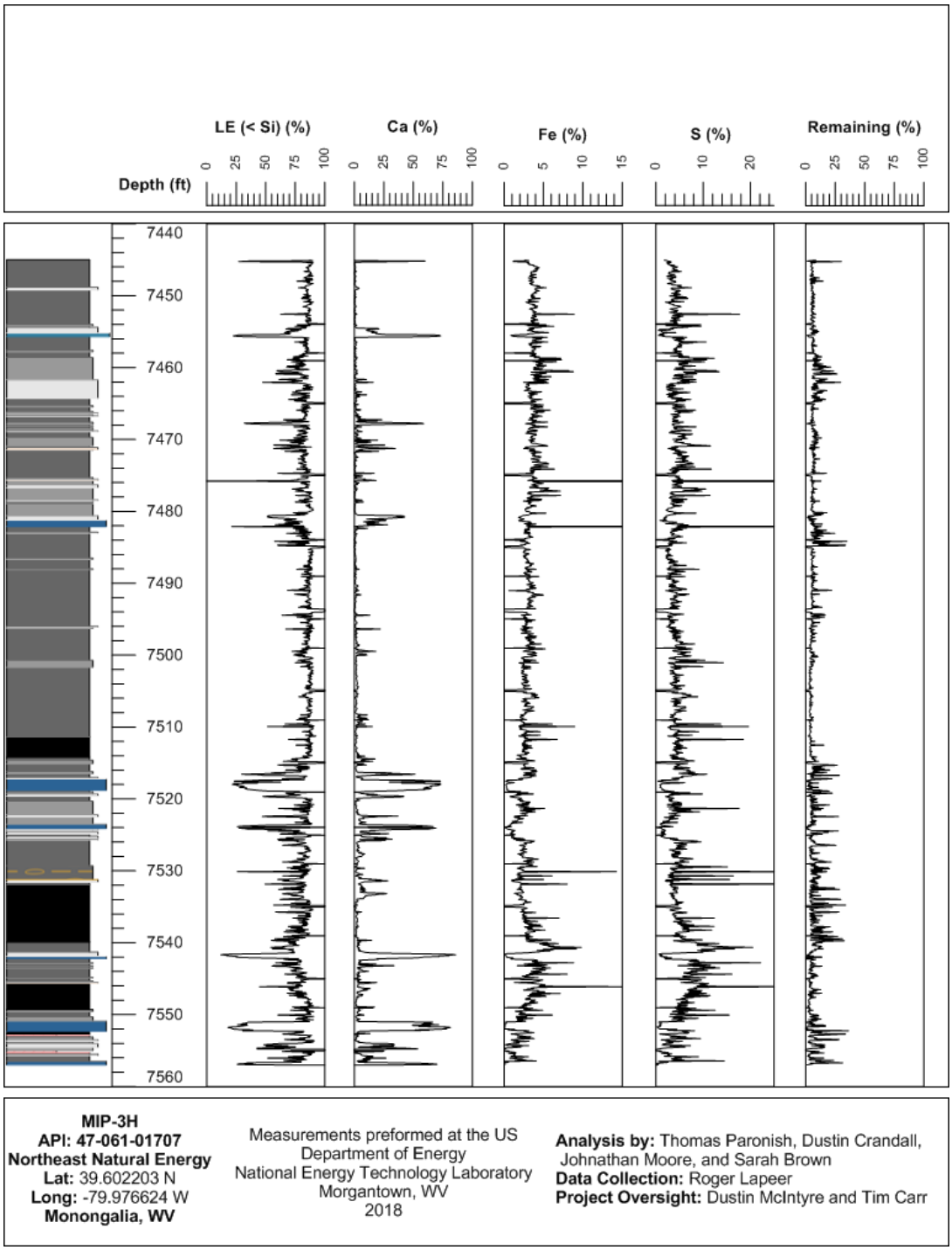

Figure 40: Compiled core log detailing the Soil Suite elemental results; column 1: Strat. column (see Figure 5 for lithology key), 2: light elements (up to silicon) (LE) (%), 3: calcium (Ca) (%), 4: iron (Fe) (%), 5: sulfur (S) (%), and 6: remaining elements contribution (%).

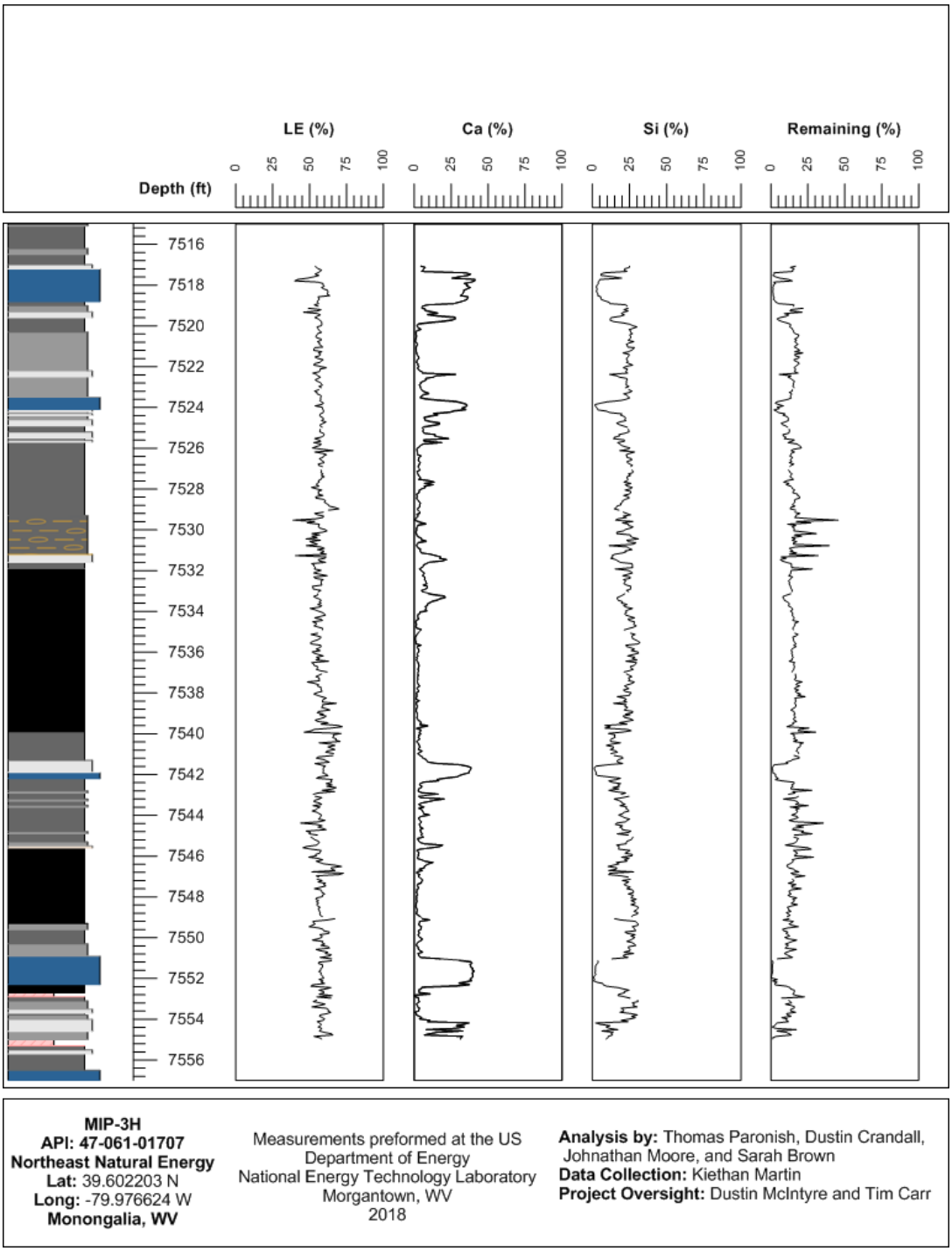

Figure 41: Compiled core log detailing the Mining-Plus Suite elemental results; column 1: Strat. column (see Figure 5 for lithology key), 2: light elements (up to silicon) (LE) (%), 3: calcium (Ca) (%), 4: silicon (Si) (%), and 5: remaining elements contribution (%).

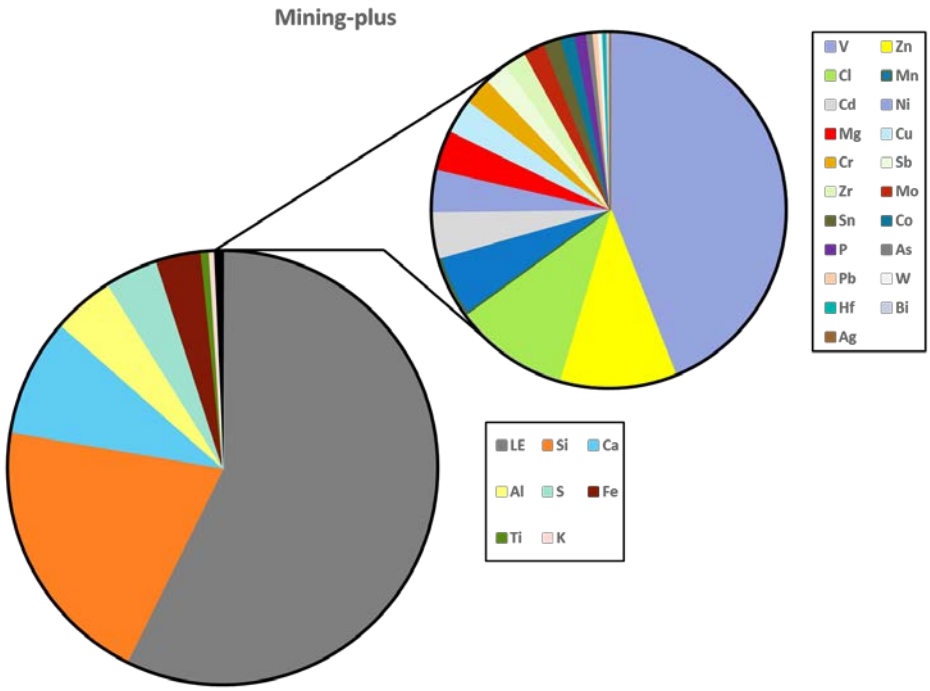

Figure 42: Total elemental proportions of the Mining-Plus Suite; secondary pie chart represents 0.3% of the total.

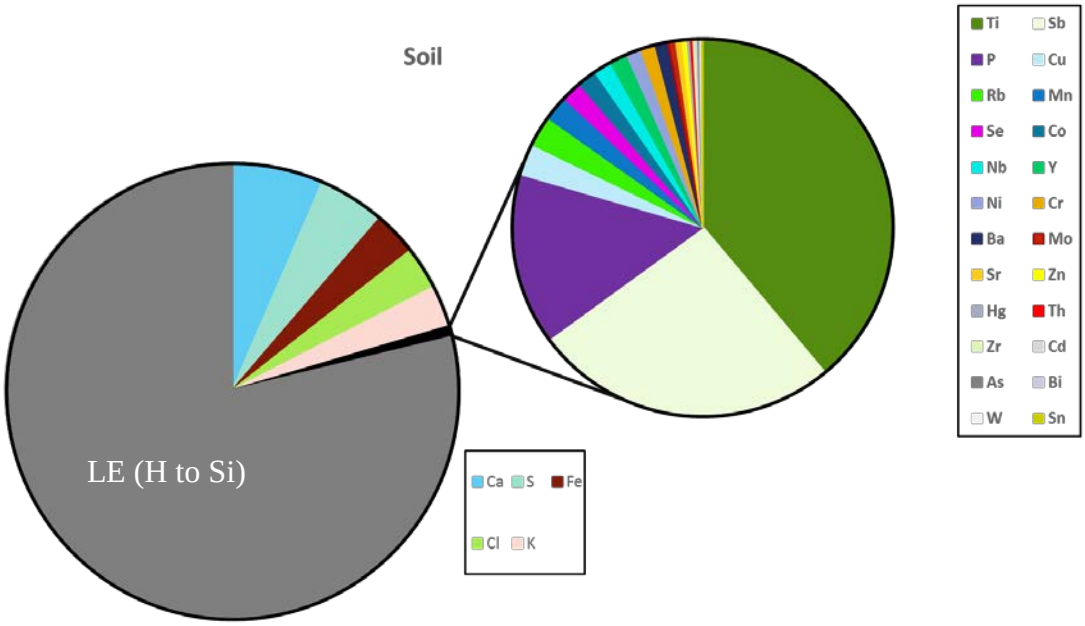

Figure 43: Total elemental proportions of the Soil Suite; secondary pie chart represents 0.75% of the total.

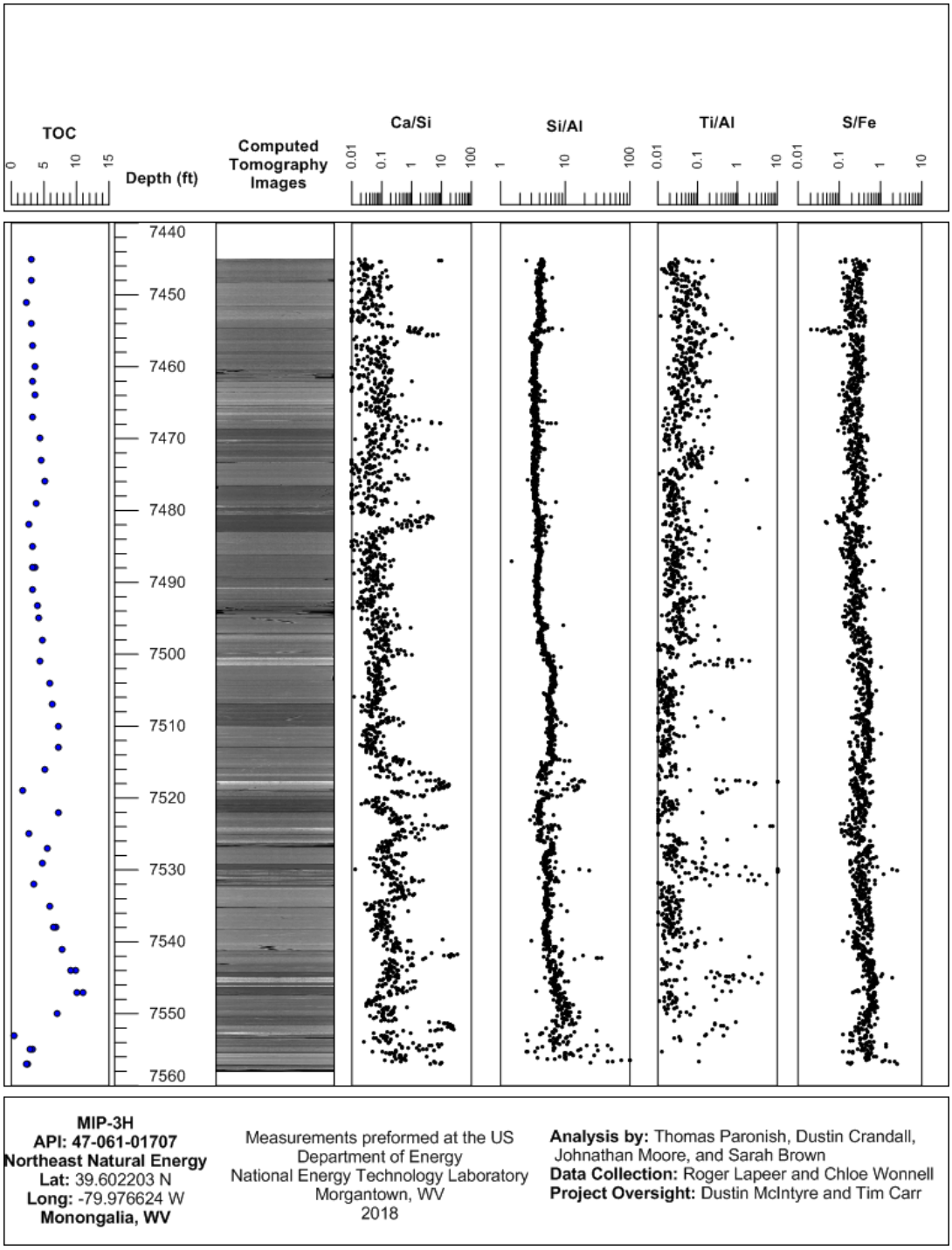

Figure 44: Compiled core log with elemental ratios from Mining Suite; column 1: total organic carbon (wt%), 2: CT images, 3: Ca/Si ratio, 4: Si/Al ratio, 5: Ti/Al ratio, and 6: S/Fe ratio.

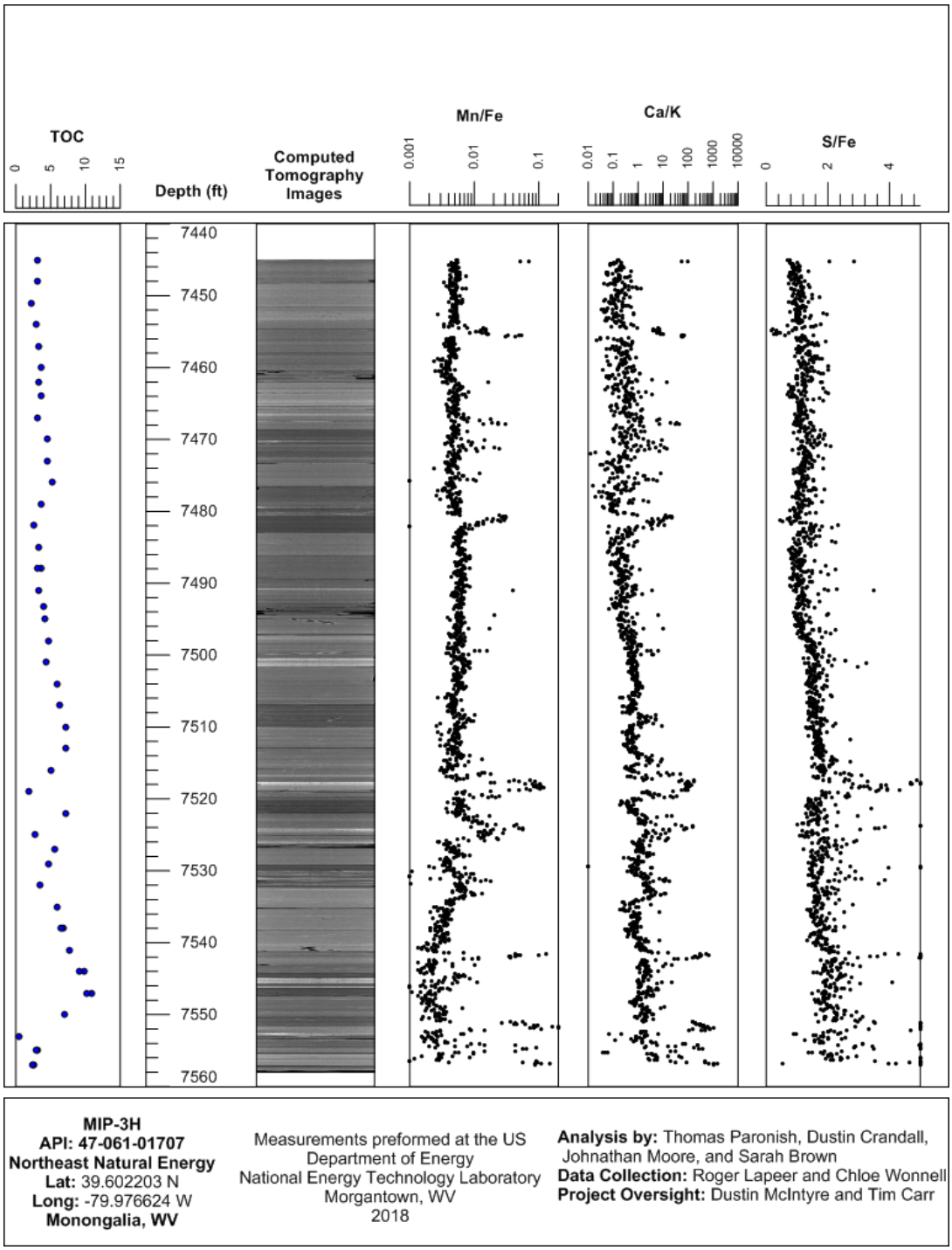

Figure 45: Compiled core log with elemental ratios from Soil Suite; column 1: total organic carbon (wt%), 2: CT images, 3: Mn/Fe ratio, 4: Ca/K ratio, and 5: S/Fe ratio.

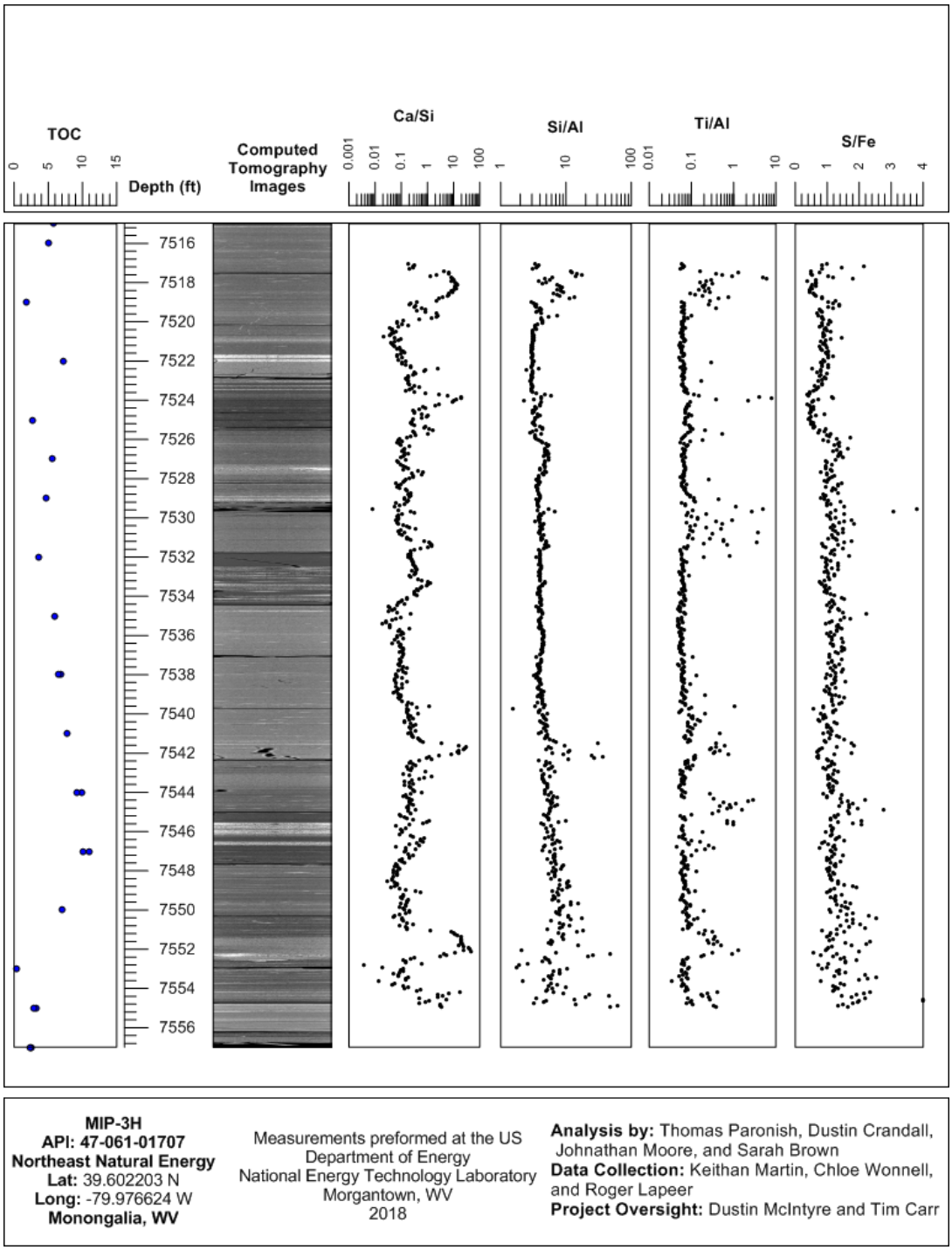

Figure 46: Compiled core log with elemental ratios from Mining-Plus Suite; column 1: total organic carbon (wt%), 2: CT images, 3: Ca/Si ratio, 4: Si/Al ratio, 5: Ti/Al ratio, and 6: S/Fe ratio.

5. DISCUSSION

The incorporation of the MSCL, CT scanning, and traditional sample analysis provides a multidisciplinary sample evaluation approach and allows for the development of a comprehensive and systematic sample analysis methodology. Use of these techniques in sample evaluation will allow for more consistent and robust data production at NETL.

XRF quality was investigated comparing the MSCL handheld suites to energy dispersal XRF (Hamilton Suite). This analysis shows that the handheld XRF quality is the best in the Mining-Plus Suite, which has the greatest accuracy of the three suites. Evidence for this is shown through moderate/strong correlations between like elements (Ca, Mo, Ni, Cu, Zn, Al, K, Si, Cr, Fe, and As) in the Hamilton and Mining-Plus Suite. The moderate/strong correlations are likely attributed to the increase in exposure time in all elements, especially in the case of the trace elements (e.g. Mo, Zn, Ni) which have stronger correlations in Mining-Plus Suite compared to the Soil Suite. Additionally, poor correlations can also be attributed to the handheld tools detection limits (e.g. Mg and P) and loss on ignition of volatile elements in the Hamilton Suite (e.g. S).

The results of the MSCL and CT analysis shows an increase in detrital influence with ascending depth. This trend corresponds with a decrease in TOC, decrease in the frequency of carbonate intervals, and decrease in pyrite content. The overall redox state in the cored interval is anoxic, with smaller scale variation between anoxic/euxinic and oxic/dysoxic.

6. REFERENCES

Blakey, R. Middle Devonian (385Ma), North American Paleography, 2010. https://www2.nau.edu/rcb7/ (accessed December 14, 2018).

Boyce, M. L.; Carr, T. R. Lithostratigraphy and petrophysics of the Devonian Marcellus interval in West Virginia and southwestern Pennsylvania. In Conference Proceeding Presented at the GCSSEPM Foundation Bob F. Perkins Research Conference, Houston, Texas, USA, December 2009.

Brett, C. E.; Baird, G. C. Middle Devonian Sedimentary Cycles and Sequences In The Northern Appalachian Basin. *Special Papers-Geological Society of America* **1996,** 213–242.

Cnudde, V.; Boone, M. N. High-resolution X-ray computed tomography in geosciences: A review of the current technology and applications. *Earth-Science Reviews* **2013,** *123*, 1–17.

Energy Information Administration, EIA. Oil and Gas Supply Module. *Assumptions to Annual Energy Outlook 2018*; p 1–19.

Ettensohn, F. R. Controls on development of Catskill Delta complex basin-facies. *Geological Society of America Special Papers* **1985,** *201*, 65–78.

Geotek Ltd. Multi-Sensor Core Logger Manual; Version 05-10; Published by Geotek, 3 Faraday Close, Daventry, Northamptonshire NN11 8RD, 2010. info@geotek.co.uk, www.geotek.co.uk

Hupp, B. N. Provenance of the Hamilton Group: A Study of Source-to-Sink Relationships within the Middle Devonian Central Appalachian Basin. Master's Thesis, Eberly College of Arts and Sciences at West Virginia University. 2017; Order No. 10608023.

Hupp, B. N.; Donovan, J. J. Quantitative mineralogy for facies definition in the Marcellus Shale (Appalachian Basin, USA) using XRD-XRF integration. *Sedimentary Geology* **2018,** *371*, 16–31.

IEDA (Interdisciplinary Earth Data Alliance). SESAR, the System for Earth Sample Registration, 2018. http://www.geosamples.org/about (accessed Feb 8, 2018).

Lash, G. G.; Engelder, T. Thickness trends and sequence stratigraphy of the Middle Devonian Marcellus Formation, Appalachian Basin: Implications for Acadian foreland basin evolution. *AAPG Bulletin* **2011,** *95*, 61–103.

Lazar, O. R.; Bohacs, K. M.; Macquaker, J. H.; Schieber, J.; Demko, T. M. Capturing Key Attributes of Fine-Grained Sedimentary Rocks in Outcrops, Cores, and Thin Sections: Nomenclature and Description Guidelines. *Journal of Sedimentary Research* **2015,** *85*, 230–246.

Rasband, W. S.; ImageJ. U.S. National Institutes of Health: Bethesda, MD, 1997–2016, http://imagej.nih.gov/ij/ (accessed 2017).

Sommer, C.; Strähle, C.; Köthe, U.; Hamprecht, F.A. ilastik: Interactive Learning and Segmentation Toolkit. *Proceedings Eighth IEEE International Symposium on Biomedical Imaging (ISBI)* **2011,** 230–233.

Williams, H.; Hatcher, R. D. Suspect Terranes and Accretionary History of the Appalachian Orogen. *Geology* **1982,** *10*, 530–536.

Witzke, B. J.; Heckel, P. H. Paleoclimatic indicators and inferred Devonian paleolatitudes of Euramerica. *Canadian Society of Petroleum Geologist Memoir* **1988,** *14*, 49-63.

Wonnell, C. S. Lithofacies and Sequence Stratigraphy of the Middle Devonian Marcellus Formation for a Cored Well in Clearfield County, Pennsylvania Using Core Analysis Methods. Master's Thesis, Eberly College of Arts and Sciences at West Virginia University, Morgantown, WV, 2015.

Brian J. Anderson
Director
National Energy Technology Laboratory
U.S. Department of Energy

Jared Ciferno
Associate Director
Oil and Gas
Technology Development & Integration Center
National Energy Technology Laboratory
U.S. Department of Energy

Elena Melchert
Director
Division of Upstream Oil and Gas Research
U.S. Department of Energy

Bryan Morreale
Executive Director
Research & Innovation Center
National Energy Technology Laboratory
U.S. Department of Energy

NETL Technical Report Series